



Kent Academic Repository

Tucker, Paul William John Luke (2022) *The Synthesis, Characterisation and Electroanalysis of Organic Redox Active Molecules*. Master of Science by Research (MScRes) thesis, University of Kent,.

Downloaded from

<https://kar.kent.ac.uk/93684/> The University of Kent's Academic Repository KAR

The version of record is available from

<https://doi.org/10.22024/UniKent/01.02.93684>

This document version

UNSPECIFIED

DOI for this version

Licence for this version

CC BY (Attribution)

Additional information

Versions of research works

Versions of Record

If this version is the version of record, it is the same as the published version available on the publisher's web site. Cite as the published version.

Author Accepted Manuscripts

If this document is identified as the Author Accepted Manuscript it is the version after peer review but before type setting, copy editing or publisher branding. Cite as Surname, Initial. (Year) 'Title of article'. To be published in *Title of Journal*, Volume and issue numbers [peer-reviewed accepted version]. Available at: DOI or URL (Accessed: date).

Enquiries

If you have questions about this document contact ResearchSupport@kent.ac.uk. Please include the URL of the record in KAR. If you believe that your, or a third party's rights have been compromised through this document please see our [Take Down policy](https://www.kent.ac.uk/guides/kar-the-kent-academic-repository#policies) (available from <https://www.kent.ac.uk/guides/kar-the-kent-academic-repository#policies>).

The Synthesis, Characterisation and Electroanalysis of Organic Redox Active Molecules

By

Paul William John Luke Tucker

Submitted:

March 2021

Submitted to:

University of Kent

School of Physical Sciences

For the degree of:

MSc Chemistry via Research

Primary Supervisor: Dr. Alexander Murray
Secondary Supervisor: Dr. Christopher Serpell

Abstract

With global efforts to shift to renewable energy sources increasing, the requirement for cheap, sustainable, and effective energy storage solutions have increased also. Current battery technologies are limited both by their reliance on finite resources and versatility, flow battery technologies such as those seen in currently deployed vanadium redox flow batteries (VRFBs) offer an alternative to traditional energy storage solutions but are still dependant on a financially volatile and finite commodity. Novel organic redox flow batteries (ORFBs) present a sustainable alternative to current flow battery systems, however are hindered by their performance, cost, and often are not derived from sustainable sources. This paper seeks to find an organic redox active molecule with the versatility to operate effectively within a range of conditions. The most promising molecule was found to be a water soluble anionic alloxazine (**11d**) derived from riboflavin – which presents a redox potential of -0.774 V in unbuffered acidic conditions and -0.907 V in unbuffered neutral conditions vs. an Ag/AgCl reference electrode making it suitable as an anolyte within flow battery systems. This molecule was shown to operate in a flow battery setup coupled with HBr/Br₂ in acidic conditions with an E_{cell} value of 1.818 V and a maximum observed current efficiency of ~44 % and a capacity fade of ~20 %.

Acknowledgements

University of Kent, School of Physical Sciences *now* Division of Natural Sciences

Dr. Alex Murray – *University of Kent* – Lecturer in Chemistry - Primary Supervisor

Dr. Chris Serpell – *University of Kent* – Reader in Chemistry - Secondary Supervisor

Dr. Ewan Clark – *University of Kent* - Director of Undergraduate Studies for Chemistry

Antigoni Pépés – *University of Kent* - PhD Student

Contents

Abstract	2
Acknowledgements	2
Table of Contents	3
List of Abbreviations	4
Compound List	5
Chapter 1: Background	6-36
Chapter 2: Aims	37
Chapter 3: Results and Discussion	38-68
Chapter 4: Conclusions	69-71
Chapter 5: Experimental Methodology	72-82
Bibliography	83-86

List of Abbreviations

Abbreviation	Meaning
b (FTIR)	Broad
CV	Cyclic Voltammetry
d (NMR)	Doublet
DCM	Dichloromethane
dd (NMR)	Doublet of doublets
DMF	Dimethylformamide
DMSO	Dimethyl sulfoxide
EPDM	Ethylene propylene diene monomer
FPM	Fluorocarbon Rubber
FTIR	Fourier Transform Infrared Spectroscopy
h	Hours
m	Minutes
NMR	Nuclear Magnetic Resonance Spectroscopy
PTFE	Polytetrafluoroethylene
q (NMR)	Quartet
RFB	Redox Flow Battery
s (FTIR)	Sharp
s (NMR)	Singlet
SCE	Saturated Calomel Electrode
SHE	Standard Hydrogen Electrode
SOC	State of Charge
SSE	Solid State Electrolyte
t (NMR)	Triplet
THF	Tetrahydrofuran
UV/Vis	Ultraviolet/Visible Spectroscopy
VRFB	Vanadium Redox Flow Battery

Compound List – IUPAC Names

Compound Label	IUPAC Name
1a	9,10-dioxoanthracene-2,6-disulfonate
1b	4,4'-((9,10-dioxo-4a,9,9a,10-tetrahydroanthracene-2,7-diyl)bis(oxy))dibutyric acid
1c	1,8-bis(2-(2-(2-hydroxyethoxy)ethoxy)ethoxy)anthracene-9,10-dione
1d	2,6-dihydroxy-4a,9a-dihydroanthracene-9,10-dione
1e	2,3,6,7-tetrahydroxy-4a,9a-dihydroanthracene-9,10-dione
2a	Disodium 4,5-dihydroxybenzene-1,3-disulfonate
3a	N',N'-dimethyl-4,4'-bipyridinium
3b	N',N'-diethyl-4,4'-bipyridinium
3c	N',N'-dibenzyl-4,4'-bipyridinium
3d	3a - 3 Unit Assembly
3e	3a - 5 Unit Assembly
3f	3a - 13 Unit Assembly
3g	1,1'-Bis[3-(trimethylammonio)propyl]-4,4'-bipyridinium
4a	(2,2,6,6-Tetramethylpiperidin-1-yl)oxyl ⁺
4b	4-Hydroxy-2,2,6,6-tetramethylpiperidinoxy
4c	4-[3-(trimethylammonio)propoxy]-2,2,6,6-tetramethylpiperidine-1-oxyl
4d	(2,2,6,6-Tetramethylpiperidin-1-yl)oxyl
4e	1,4-dihydroxy-2,2,6,6-tetramethylpiperidin-1-ium
5a	Phenazine
6a	7,8-Dimethyl-10-[(2S,3S,4R)-2,3,4,5-tetrahydroxypentyl]benzo[g]pteridine-2,4-dione
6b	(2R,3S,4S)-5-(7,8-Dimethyl-2,4-dioxo-3,4-dihydrobenzo[g]pteridin-10(2H)yl)-2,3,4-trihydroxypentyl dihydrogen phosphate
6c	[(2R,3S,4R,5R)-5-(6-Amino-9H-purin-9-yl)-3,4-dihydroxytetrahydro-2furyl]methyl (2R,3S,4S)-5-(7,8-dimethyl-2,4-dioxo-3,4-dihydrobenzo[g]pteridin-10(2H)-yl)-2,3,4-trihydroxypentyl dihydrogen diphosphate
7a	Benzo[g]pteridine-2,4(1H,3H)-dione
7b	2,4-dioxo-1,2,3,4-tetrahydrobenzo[g]pteridine-x-carboxylic acid
8a	5-(tert-butyl)-2-(tert-butyl(aminoxyl)benzoic acid
9a	2-Methyl-2-nitrosopropane
10a	2-(tert-butyl(aminoxyl)-2-phenylacetic acid
11a	7,8-Dimethylbenzo[g]pteridine-2,4(1H,3H)-dione
11b	2,2'-(7,8-dimethyl-2,4-dioxobenzo[g]pteridine-1,3(2H,4H)-diyl)bis(N,N,N-trimethylethan-1-aminium)
11c	4,4'-(7,8-dimethyl-2,4-dioxobenzo[g]pteridine-1,3(2H,4H)-diyl)bis(butane-1-sulfonate)
11d	4,4'-(7,8-dimethyl-2,4-dioxobenzo[g]pteridine-1,3(2H,4H)-diyl)bis(propane-1-sulfonate)

Chapter 1 – Background

There is an ever increasing need to provide a cheap and sustainable method of storing energy due to global efforts into replacing fossil fuel options with renewable energy alternatives. These alternatives may only operate intermittently, such as solar only being able to operate in the daytime and depending on the technology implemented may be at a reduced efficiency due to certain environmental factors such as cloud coverage. As well as wind energy solutions, requiring adequate wind speeds to be able to drive the rotors and thus produce electricity. Such efforts are evident, with the UK aiming to achieve a goal of being able to supply 15% of its energy consumption by 2020 from renewable sources, this translates into an operational capacity of 29 GW.^[1] In the ‘UK Renewable Energy Roadmap’^[1], published in 2011 it is outlined that the costs of these renewable energy technologies are uncertain. This includes not only implementing the production technology, but in tandem the complimentary updated grid systems that are required as well. Providing an energy storage solution that could solve the problem of high cost, whilst being sustainable would be perfectly complimentary to this goal. Current storage technologies range from hydroelectric in the form of pumped water and hydroelectric dams, mechanical storage such as flywheel systems and battery storage, such as molten-salt batteries and modern flow battery technologies. This work focuses mainly on battery storage systems, specifically currently implemented flow battery technologies and alternatives to these systems.

There are fundamental operating differences between redox flow batteries and conventional batteries. Conventional batteries for example Li-Ion batteries work by housing two separate electrodes in their solid states, with the movement of charged lithium ions between these electrodes producing a current.^[2] The direction in which these lithium ions move is dependent on if the system is being charged or discharged. On the other hand redox flow batteries work via two separate electrolytic solutions being cycled around fluid circuits by pumps as seen

below in Figure 1. Housed in the fluid circuit are two porous electrodes divided by an ionexchange membrane. This membrane is ultimately where the movement of single ions is facilitated; the direction in which ions are being transferred depends on whether the system is being charged or discharged. It is this movement of ions that facilitates the movement of electrons around an external circuit. This circuit is connected to the previously mentioned porous electrodes where the respective half-reactions of the two mediators take place. [3]

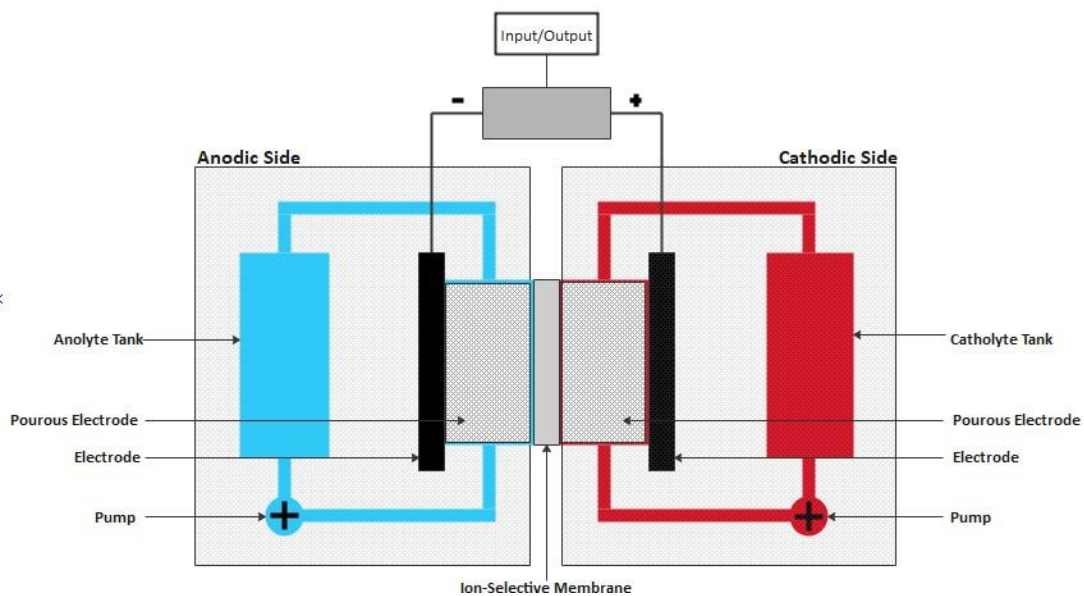


Figure 1 - Typical Flow Battery Diagram

These systems rely on the redox-active nature of certain metal ions or molecules in liquid electrolytes, either symmetrically with both the positive and negative electrolyte consisting of the same species of molecule or ion (e.g. $V^{II/III}|V^{V/VI}$) or unsymmetrically with the positive and negative electrolyte consisting of different species of molecules or ions. (e.g. $Zn/Zn^{2+}|Br_2/2Br$).

There are several key factors that are focused on when searching for an energy storage solution to replace current grid-storage facilities:

Cost: Current projections for Flow Battery Systems see them exceeding the cost of traditional battery systems and alternate energy storage systems alike. [4] RFBs must be financially viable

to implement and maintain if these new storage options are too costly companies will not favour implementing such systems over current industry standards.

Scalability: These systems must be able to be scaled either up or down to meet required needs.

The capacity of a flow battery system is directly correlated to the volume of the electrolyte. ^[5]

This enforces a ceiling on capacity only limited by the size of the facility in which the system is housed. This is thus, directly linked to cost. With an increased system capacity, it drives the price of deploying said system up by means of land acquisition and construction costs for a facility.

Cycle Efficiency: Many conventional batteries, like the Li-ion batteries that are found in almost all handheld electronic devices in present day have a limited lifetime. Ultimately, how many times they can be charged and discharged before their capacity eventually depletes until the battery no longer functions. ^[6] Having a battery that will last over multiple years, worth of these cycles once implemented, is again a necessity and as such finding an alternative solution that matches or exceeds the lifetime of a Li-ion battery is key.

Sustainability: With the global energy sector steering towards renewable energy sources utilising wind and solar energy production methods ^[7], the use of finite resources such as lithium, cobalt and lead in the storage of energy from these renewable sources, may be counterproductive in reducing the environmental impact of using these production methods. Providing a method of energy storage as such to utilise readily available and naturally occurring organic molecules would give an alternative to using these finite resources.

Current research into all manner of flow battery systems aims to minimise and maximise these respective key factors. Doing so may ultimately provide a sustainable, cheaper, and more efficient method of energy storage.

Certain classes of redox flow battery such as those that utilise vanadium have already been implemented in some parts of the world as grid-scale storage alternatives^[8] as well as variants that utilise zinc/bromine being installed in residences.^[9]

Redox flow batteries can be split into organic and inorganic categories. Redox flow batteries can also be used with a combination of organic^[10] and/or inorganic ions^[11], or metal ions with organic ligand complexes.^[12]

1.1 Inorganic Redox Flow Batteries

As previously outlined these inorganic systems rely on the ability of certain metal ions to exist in multiple oxidation states, the most prominent and implemented example of these systems being the vanadium redox flow battery. Vanadium systems have already implemented as gridstorage alternatives across the globe, with China playing a leading role in the installation of these batteries^[14], it is clear that the technology for inorganic flow battery systems at least, can compete with current grid-storage options. Within this subsection different species of inorganic systems will be described from both current research and implemented examples and compared to not only each other but of the performance of conventional batteries as well.

1.1.1 Vanadium Redox Flow Batteries

This class of flow battery utilises the fact that vanadium can exist in multiple oxidation states, and is perhaps the most widely used chemistry in current redox flow batteries. Due to these systems boasting the most promising characteristics in terms of cycle life and energy density, they are the most heavily researched.^{[11][13]} They operate by housing vanadium in different oxidation states in two separate tanks. The electrolytic solutions of vanadium, one positive; usually VO_2^+ and one negative; usually $\text{V}^{2+/3+}$ are circulated through respective half cells where these reactions take place, these are shown below in Figure 2.

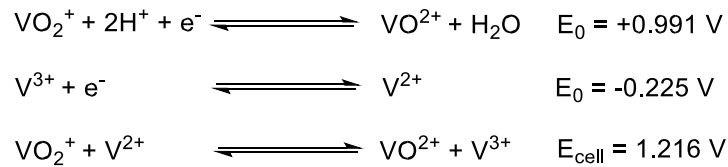


Figure 2- Half Cell and Overall reaction/s of a Vanadium Flow Battery – Potentials reported vs. SHE

During charging, the V^{3+} species is reduced to V^{2+} and the VO_2^+ species is oxidised to VO^{2+} .

During discharging, this process is reversed. ^[11]

Implemented examples of these systems are tailored to different applications, and as such vary in their capacity. The ‘Avista Regional Grid Energy Storage’ implemented in the USA in 2015 and houses a maximum power of 1.2 MW and a maximum capacity of 3.2 MWH and is composed of multiple battery modules each with a capacity of 60KW. This system is aimed at improving the efficiency of the regional power grid by methods of peak load shifting and voltage support. ^[8] Implemented at a larger scale, is the system located in Dalian in the Liaoning Province, China. This system houses a maximum power of 200 MW and a maximum capacity of 800 MWH and is composed of their multiple battery modules with a capacity of 500 KW each. The system is aimed at ensuring there is adequate power during important load times and serving as an auxiliary power supply for ‘black starts’; a process of restoring a power station without relying on an external power transmission network to recover from the downtime. ^[14]

Residential examples of VRFB systems are being fielded, with companies such as ‘VoltStorage GmbH’ promoting VRFB systems for use in private residences. Their ‘VoltStorage Smart’ product offers a storage system that is ideally used with residential photovoltaic systems, to offer ‘energy independence’ and move its users more off-grid. With each of their units boasting a capacity of 6.2 kWh with a total continuous power of 1.5 kW, it

is worth noting that these units can be connected in series to increase both of these values, dependent on need. These systems are also graded to have a ‘100% capacity guarantee’ for a length of 10,000 charging cycles. ^[15]

Current research examples exist as this technology is being built upon to further improve the desired characteristics of the systems. With further advancements fine tuning properties and consistencies of the system. Such examples include the use of sulfate-chloride mixed solutions to best improve the solubility of the vanadium species within the electrolytes. ^[16]

Currently, vanadium-based systems provide the most promise in respects to the operation characteristics such as specific energy and energy density. This increased level of attention has resulted in larger developments and improvements for these systems. With a cycle-life ranging from 12000 to 14000 cycles, converting into a calendar life of roughly 20 years, this translates to cycle-lives that exceed that of some Li-ion systems and calendar lives that at least match the current average for Li-ion systems. Currently the energy density of these systems ranges from 15-70 WhL⁻¹. ^[13] However, Li-ion technologies face scalability issues and as previously stated redox flow batteries can be scaled as required. In addition, all of the vanadium that is used in these systems can be repurposed once the battery is decommissioned. Due to the aqueous nature of these systems and the fact that they house a water-based electrolyte, this makes them very safe to work with; there are no flammability hazards as there are with Li-ion systems, meaning these vanadium systems are safe to implement on large scale and deploy them in populated areas.

These systems, however, are not without their disadvantages. Vanadium can be found in numerous different minerals and is a by-product of the steel industry, through the processing of magnetite iron ores. ^[17] As a result of this naturally occurring scarcity and the main source

coming from an unrelated industry, just like any commodity market the price of vanadium fluctuates over time; thus, during certain periods steel production and therefore unit price of vanadium may increase or indeed decrease. ^[18] Vanadium itself is therefore a finite resource, and as such its price may increase in relation to a potential increased scarcity. The elemental form of vanadium is not considered toxic; however, repurposed electrolyte has the potential to form vanadium(V) oxide, which is mutagenic, toxic, and hazardous to the environment. ^[19] Additionally vanadium systems house solutions that have the potential to form acutely toxic soluble vanadates such as sodium metavanadate. ^[20]

1.1.2 Iron Chromium Redox Flow Batteries

Systems utilising the $\text{Fe}^{2+}/\text{Fe}^{3+}$ and $\text{Cr}^{2+}/\text{Cr}^{3+}$ couples were first developed and published by NASA in 1974 making them a predecessor to the modern flow systems that are utilised in some grid-scale applications today. This system relied on the use of hydrochloric acid as to stabilise metal chloride salts during operation. The implementation of the system saw researchers select redox couples so that the electrolysis of water did not occur. This electrolysis typically occurs at a minimum voltage of 1.23 V and the rate at which water is electrolysed increases beyond this. This selection is evident from a low cell voltage in this specific example, the relevant half-

equations and full cell equations are shown below in Figure 3. ^[21]

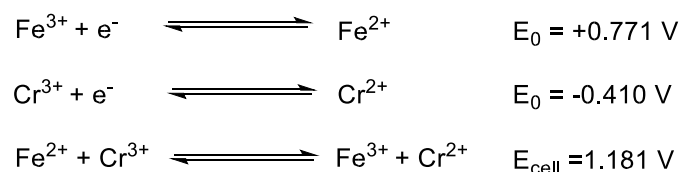


Figure 3 - Half Cell and Overall reaction/s of a Fe/Cr Redox Flow Battery – Potentials reported vs. SHE

These systems have been subject to further optimisation studies, focusing on changing the operating parameters to best enhance the positive characteristics of the system. With the development of membranes better suited for these specific applications and as a result of these optimisation studies, figures of 97% coulombic efficiency and 73% energy efficiency were published in 1991 based on finding an ideal electrolyte composition, operating temperature and membrane for the operation of the system. [22]

Larger scale versions of these systems are known. In a peer review published by the United States of America, Department of Energy in 2014; entitled ‘Long-Duration, Grid-Scale Iron/Chromium Redox Flow Battery Systems’, plans to implement the first ever MWh-scale Fe/Cr redox flow battery are highlighted. This system was ultimately placed into operation in 2014, with the hope that it would ease peak demand issues in Sunnyvale, California. Within the charge and discharge cycles of this system, it is presented in this review that each cell that made up this system was stable and displayed ‘excellent uniformity’ meaning that each cell was charging at a similar rate. Cell uniformity in these types of grid-scale systems is important as to not overload individual cells and ultimately lose energy that is put into a ‘full’ cell. The impact of this program is highlighted to not only reduce blackouts by providing an energy store for peak operating periods but in general stabilise the existing grid network. [23]

More recent research examples of these systems seek to improve and build on the success of the Fe/Cr system, with various groups focusing research efforts into adjusting the operating conditions of these systems by the design of differing metal complexes. A paper published in February 2020 highlights the design of new chromium complexes as to achieve Fe/Cr operation in neutral conditions and to address the issues of both parasitic reactions that occur in these types of systems, and to overcome the slow kinetics of the system. The result of this new chromium complex yielded an increase of the existing solubility to 0.7 M in a system that

was coupled with ferrocyanide and illustrates a capacity fade from ~26 mAh to ~23 mAh over a period of 100 cycles. ^[24]

A comparative study published in 2015, conducted between vanadium redox flow systems to iron-chromium systems and their applications in large-scale energy storage. This paper compares each of the types of system based on various performances such as: Charge/Discharge efficiency, cycle life and cost-efficiency. Both systems are reported to have similar energy efficiencies at high current densities, whereas iron-chromium systems exhibit a higher capacity decay than vanadium systems, meaning that these systems will not last as long when in operation. However, in terms of cost-efficiency it is reported that iron-chromium systems are cheaper than vanadium systems to implement when operated at high power densities and/or larger capacities. ^[25]

1.1.3 Actinide Redox Flow Batteries

In 1999, a paper entitled ‘An Application of Actinide Elements for a Redox Flow Battery’ ^[26], by Yoshinobu Shiokawa proposing the idea of actinides such as uranium and neptunium as by-products from nuclear reactors to be repurposed and utilised in flow cell systems. This work concluded in stating the feasibility of using these elements in these types of systems. Observing that the chemical properties of the actinides; U, Np, Pu and Am are comparable to that of vanadium for example and given the success of these vanadium systems, the potential to utilise certain actinide elements is there. A later paper published in 2006 by Shiokawa, described the energy efficiency of such redox flow systems that utilised both U and Np. ^[27]

This example of a uranium system utilises uranium acetylacetonate, due to its high solubility within aprotic solvents and its potential gap between $U^{III/IV}$ and $U^{V/VI}$. With a charging process and a complete redox reaction shown below in Figure 4.

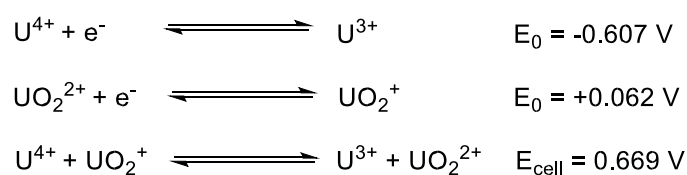


Figure 4 - Half Cell and Overall reaction/s for a Uranium Flow Battery – Potentials reported vs. SHE

Furthermore, the example put forward for a neptunium system indicates that there are four oxidation states of Np which are soluble in aqueous solutions, those being: $\text{Np}^{\text{III/IV}}$ and $\text{Np}^{\text{V/VI}}$, utilising glassy carbon electrodes and nitric acid as an aqueous medium a cell voltage of ~ 1 V is reported, however the half-cell potential for NpO_2^{+} can only be estimated at either -0.853 V or $+1.147$ V based on E_{cell} . With the two half equations and a complete redox reaction being shown below in Figure 5.

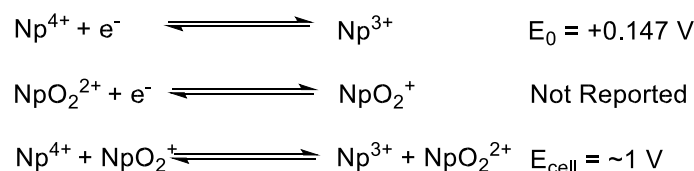


Figure 5 - Half Cell and Overall reaction/s for a Neptunium Flow Battery – Potentials reported vs. SHE

The proof of concept published in the 2006 paper provides an insight into the use of actinides in flow battery systems, with the main advantage being that it gives additional purpose to by-products of nuclear fission reactors. This one point encompasses multiple other benefits, reducing the amount of depleted uranium being held in storage facilities as uranium hexafluoride which is: still radioactive and as such can release ionising radiation, highly corrosive, reactive and possesses various toxic and mutagenic properties, making it a danger

to store in large quantities. Although this depleted uranium can be sold already once repurposed for military and commercial uses, the waste that is not sold is sent to disposal sites. By providing another alternative use for nuclear by-products the 700,000 metric tonnes of depleted UF₆ currently held in storage in the US alone, reported by the United States Nuclear Regulatory Commission ^[28] could be utilised to improve energy infrastructure. Inadvertently, reducing the amount of radioactive waste that is being stored, however site selection will have to be carefully chosen due to the radioactivity of the electrolyte within the potentially deployed flow system.

There are to be expected various disadvantages with utilising actinides, whilst they are naturally occurring; they are a finite resource with some of the elemental series being extremely scarce – the only counter to this is that discovery of new reserves and progress into different enrichment techniques is ongoing. As well as the production of neptunium occurring upon the decay of uranium itself via neutron bombardment. As with most commodities, the market for them is fluctuating relying on supply and demand; with some of the actinides being extremely expensive for example Np stands at roughly \$660,000 /kg, so the use of these expensive elements is not economically viable to purchase and only utilise waste from fission reactions.

1.2 Hybrid Redox Flow Batteries

A hybrid redox flow battery operates the same as a general redox flow system in that it houses two oppositely charged electrolytes and circulates these electrolytes around a fluid circuit and through a cell. However, one key difference defines ‘hybrid’ systems – the use of both metallic and non-metallic substances as shown below in Figure 6. This shows a generalised schematic of a Zn/Br hybrid redox flow battery and how the zinc is deposited onto the electrode.

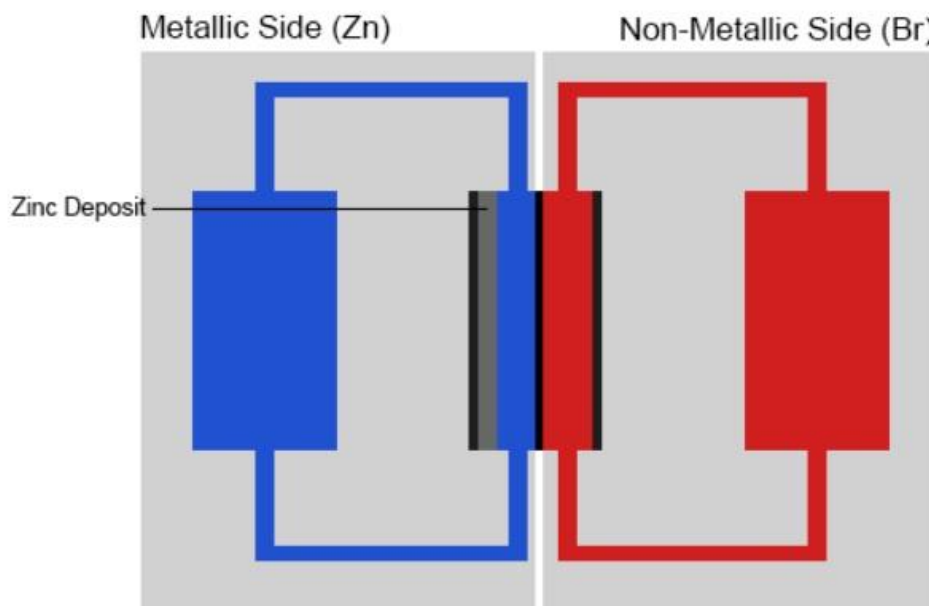


Figure 6 - Schematic Diagram of Zn/Br Flow Battery

1.2.1 Zinc/Bromine Redox Flow Batteries

Zinc Bromide flow battery systems operate slightly differently to conventional flow batteries due to the fact that on the anodic side of the cell, zinc is being electroplated onto the electrode, a process which occurs when the zinc is reduced during charging. Upon discharging, this metallic zinc is then oxidised to Zn^{2+} ions which dissolve into the aqueous anolyte, this release of electrons is what then drives the reduction of bromine (Br_2) to bromide (Br^-) ions. On the cathodic side, bromine, usually coupled with an organic amine to regulate solubility, is reduced

in a regular RFB-like operation in which a solution is flowed through a porous electrode. [29]

The half-reactions and full cell reactions are show below in Figure 7:

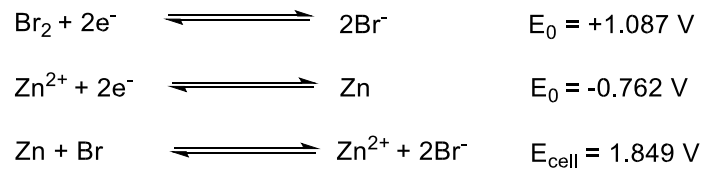


Figure 7 - Half Cell and Overall reaction/s for a Zinc Bromide Flow Battery – Potentials reported vs. SHE

Current examples such as the ‘ZBM2’ system from ‘Redflow’ [30] a company that specialises in zinc bromide systems for commercial and residential purposes, provide a 10kWh daily energy output, with an 80% energy efficiency for a 100L system – ‘Redflow’ provide a warranty of 36,500 kWh of energy delivered or a 10-year life, being that the daily energy output is 10kWh, this system would presumably last for at least 3650 cycles.

As previously mentioned, ‘Redflow’ produce two flagship products, their ‘ZBM2’ system designed for commercial uses [30] and their ‘ZCell’ system, which is designed for residential uses – ideally to be coupled with residential solar cells to charge these systems rather than connect them to grid power. These residential examples provide an insight into the fact that flow battery systems as a whole are not only limited to their uses in grid storage applications and provide an option to consumers to move partly or wholly to energy self-sufficiency in that they no longer rely on a grid network, ultimately reducing grid-load.

Current research examples, like many other research focuses on developed ideas focus on optimising and improving of the characteristics of the system to yield better outcomes. In a paper published by R. Kim et al., focusing on optimising the membrane within a Zn/Br system to thus improve the desired properties of the system. The work describes that the

implementation of treated membranes, optimising the water cluster size in place of an untreated

exchange membrane increased energy efficiency of the system by ~11%.^[31]

One of the advantages of zinc bromide systems is that 100% depth of discharge is possible, as opposed to traditional lead-acid and Li-ion batteries in which attempting this will either degrade the battery itself or cause the battery to become unstable.^[32] This value means that if the battery is charged to a given capacity in kWh, this is the amount energy that can be discharged from the battery and utilised. The ability to sustain this capacity at 100% during the lifetime of a system is paramount to its use in both commercial and residential standpoints, as a battery that is unable to deliver the full amount of energy that it is charged with is unfavourable. If this capacity decayed consistently over time, this would ultimately lead to the battery being replaced dependent on the rate of decay. Having this capacity stay relatively constant and at a value that still allows the system to remain effective extends the time between needing to replace/refurbish the system, adding to the overall cost efficiency of the system.

During the deposition of metallic zinc onto an electrode, zinc dendrites can form. The formation of these dendrites severely inhibits the systems performance, until ultimately the system fails due to forming direct contact between the anode and cathode causing a short circuit if they stay attached. If, however, the dendrites become loose and fall into the electrolytic media, this causes a decline in the capacity of the system. This effect and ways of preventing dendrite formation, however, is something that has been widely researched examples of this are the use of additives within the electrolyte. An example of these being polymers such as polyethylene glycol (PEG).^[33] These polymers work by adsorbing onto the surface of the electrode to regulate local current distribution and drives uniform zinc deposition, inhibiting the formation of dendrites. The use of these additives must be optimised

however, otherwise they may reduce certain operating parameters of the system such as voltage efficiency by

interfering with the electrochemistry of the battery. ^[33]

However, in an article outlining the ‘Redflow’ ZCell units, the price is stated at ~\$12,600 AUD per 10 kWh battery (~£6,500). This price does not include installation and the acquisition of an inverter, as well as the hardware required to already be in place to utilise and charge the storage system such as solar panels. ^[34] The capital cost of these systems may to be a negative point for consumers as opposed to relying solely on grid power from a utilities company.

However, consumer testimonials from ‘Redflow’, claim that implementation of the system had reduced their electricity bill by 80%. ^[35]

1.2.2 Zinc Cerium Redox Flow Batteries

Zinc cerium systems operate much the same as zinc bromide systems mentioned in the previous subsection. With the first zinc-cerium flow battery being developed by British company

‘Plurion Inc’, who produced a laboratory scale example. A patent issued by the USPTO (United States Patent & Trademark Office) No. US7625663B2 to Clarke et al. Working under ‘Plurion’, lists “A power cell has an electrolyte that includes a redox pair comprising of cerium.” ^[36] The patent itself goes on further to explain that the preferred electrolyte in this example is comprised of an acid electrolyte, forming an elemental ion complexed by a chelating agent. The patent also proposes a cell potential of 2.4 V for the Zn/Ce redox pair. The two half equations and overall reaction for this system is shown below in Figure 8.

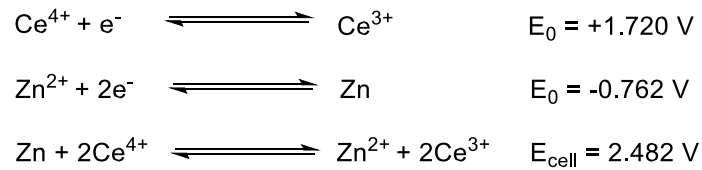


Figure 8 - Half Cell and Overall reaction/s for a Zinc Cerium Flow Battery – Potentials reported vs. SHE

Zinc-cerium systems have yet to be implemented outside of a laboratory setting, with the largest of these systems utilising a 1 m² pilot cell during testing again, by Clarke et al. This pilot cell was used during testing utilising a lead anode and discharging between 2.0 and 1.8 V, providing an average discharge power of 600 W/m². This is compared to the smaller scale cells that were also tested discharging between 1.2 and 2.2 V with power densities of between 600 and 1300 W/m². [37]

Current research examples look to improve these types of systems by further optimising their operating parameters, such as: pH, membrane type etc. A paper published in 2017, outlines the operation of a Zn/Ce system with opposite pH environments in each side of the system. This paper illustrates the zinc species being dissolved in an alkaline electrolyte on the anodic side of the cell and the cerium species being dissolved in an acidic electrolyte on the cathodic side. These two cell halves then divided by a sodium solid state electrolyte (Na-SSE) as shown below in figure 9.



Figure 9 - Equation depicting the Zn/Ce Cell Setup described in the paragraph above.

The basis of which this paper is founded is that in acidic pH zinc is subjected to corrosion and the environment seriously hinders the electrochemical potential of the zinc electrode, by dissolving the zinc species in an alkaline solution these issues are negated and improved upon, respectively. ^[38]

Although as previously mentioned, these types of systems have yet to be implemented outside of a laboratory setting. They show great promise for utilisation within flow battery systems by demonstrating the highest cell potentials when compared to other aqueous systems, making them a good choice to invest further development into as a potential alternative to currently implemented flow battery systems.

These systems however, are not without their disadvantages. Dendritic formation is a common issue within metal-based battery systems and if left unchecked can cause the complete failure of the battery. Research has been focused into development of these systems to combat the formation of zinc dendrites in these systems, with varying pH environments (mostly alkaline) to inhibit dendrite growth, which commonly occurs when utilising neutral/acidic electrolytic media - as well as the design of varying zinc salts to also prevent dendrite growth if used in neutral/acidic electrolytic media.

1.3 Organic Redox Flow Batteries

Renewable organic sources may offer a cost-effective alternative to non-renewable metal ions such as vanadium and lithium. Systems that therefore utilise these organic sources in their operation offer a battery storage alternative, which is both low in cost and sustainable in terms of its electrolyte supply. These systems operate in a similar way to those systems described in terms of flow battery technology, all-organic systems are a relatively new concept mainly being developed over the past twenty years.^[39] These organic implementations are currently being investigated primarily on a small (laboratory) scale. However, there are many examples of ongoing improvements of current organic systems and proposals for new types of these systems appearing more often in current literature. This advantage of being sourced from renewable organic sources offers a cheap alternative if these systems were to be scaled up for grid-level applications.

Organic flow batteries fall into two main categories: Aqueous and Non-Aqueous. Non-aqueous systems utilise organic solvents within the flow cell, which can have a greater environmental or toxicity impact. Aqueous systems, however, utilise water as a solvent, and can include those at neutral pH.^[40] These have the advantage of being typically more cost-efficient to their nonaqueous counterparts based on the cost between water and organic solvents. Both systems have their advantages, with those operating in non-aqueous solvents being able to present higher operating potentials.^[41]

Furthermore, these types of systems can utilise an all-organic redox couple, consisting of the use of organic molecules on both sides of the cell. Alternatively, other types of ORFB may utilise an organic-inorganic redox couple, relying on an inorganic electrolyte on one side of the cell, such as bromine or iodine.^[42] Although these organic-inorganic systems stray from

the idea of a purely organic flow battery, ultimately, they still do not include the use of metals in the system's electrolytes.

1.3.1 Quinone Based Redox Flow Batteries

These types of systems rely on the redox active nature of the organic quinone series of molecules and their derivatives. Specifically, in a recent example with system utilises **1a** and hydrobromic acid making up this redox couple. This system exhibits a two electron, two proton reduction in which **1a** is reduced to its hydroquinone counterpart and then oxidised back to the original molecule shown below in Figure 10.

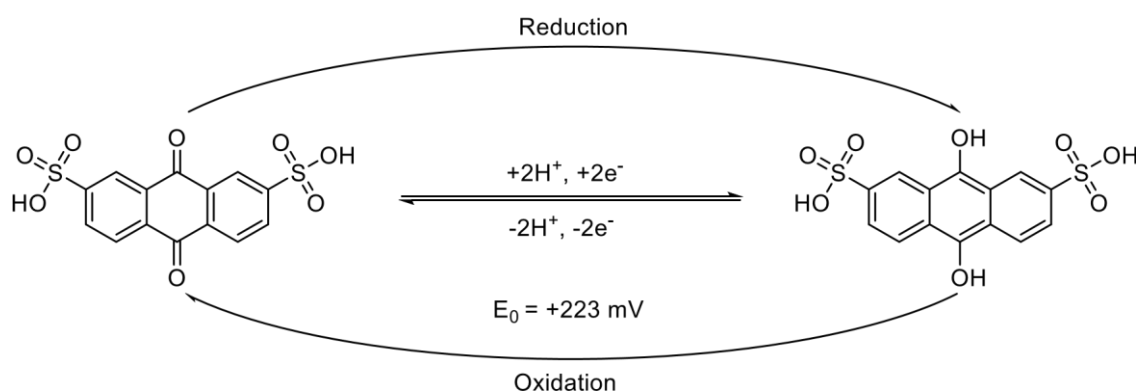


Figure 10 - Redox Pathway of **1a** – Potential recorded vs. SHE ^[42]

The above example of anthraquinone disulfonic acid coupled with hydrobromic acid, published in 2014 highlights a galvanic power density of 0.6 Wcm^{-2} at 1.3 Acm^{-2} and a capacity retention

of $>99\%$. ^[42] Furthermore, this paper demonstrates that with the insertion of two hydroxyl moieties into the structure of **1a**, the cell potential can be increased by a further 11%. Furthermore, it is reported that the open-circuit potential increased linearly from 0.69 V to 0.92 V between 10 and 90 % SOC. This system is cost effective being that anthraquinone can currently be purchased for $\sim\text{£}15/\text{kg}$ compared vanadium which stands at $\sim\text{£}19/\text{kg}$ as of December 2020.

There are also examples of quinone-based redox flow batteries operating in non-neutral conditions, specifically in alkaline conditions at pH 12. ^[43] This example utilised a carboxylate functionalised anthraquinone – **1b** shown in Figure 11 below, to best improve the solubility and stability within alkaline solutions. **1b** was tested both in symmetric cell compositions, utilising different volumes of the molecule on both positive and negative sides of the cell. As well as in a non-symmetric or full cell composition coupled with ferrocyanide. This functionality to improve solubility within different media stands testament to the versatility of various organic series and their ability to be adapted for different uses.

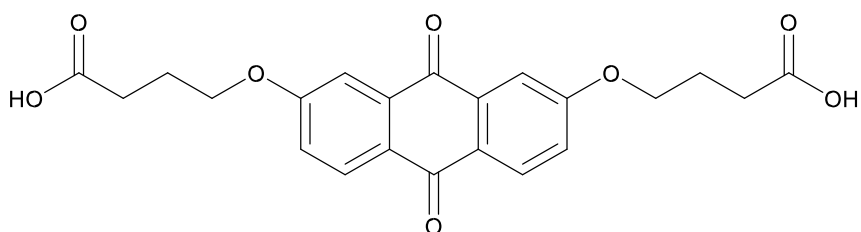


Figure 11 - Structure of Carboxylate Functionalised Anthraquinone – 1b

This is only a handful of the existing battery systems, below in Figure 12 is a more expansive list of these types of systems and the conditions in which they operate in.

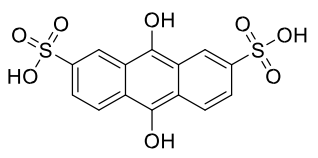
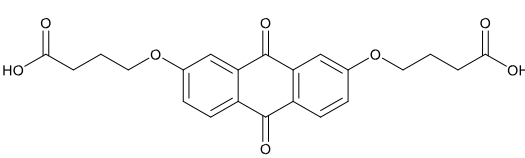
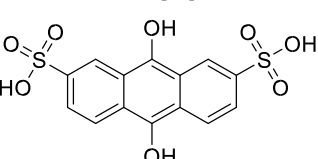
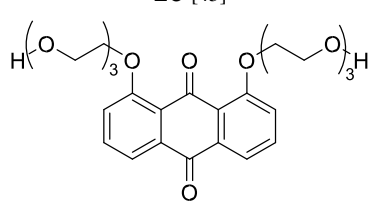
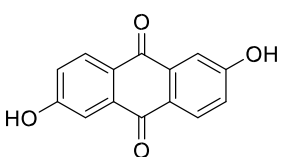
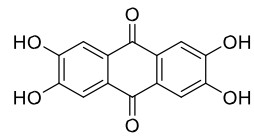
Quinone	Counter-Reaction	Conditions	E ₀ of Quinone
<p>1a [42]</p> 	HBr	Acidic	+223 mV vs. SHE
<p>1b [43]</p> 	Ferrocyanide	Alkaline	-510/-540 mV vs. SHE
<p>1a [44]</p> 	2a	Acidic	+190 mV vs. SHE
<p>1c [45]</p> 	Ferrocyanide	Alkaline Neutral Acidic	-430/-520 mV vs. SHE dependant on Polymer length and pH
<p>1d [46]</p> 	Ferrocyanide	Alkaline	-680 mV vs. SHE
<p>1e [46]</p> 	Ferrocyanide	Alkaline	-810 mV vs. SHE

Figure 12 - A Table displaying various example of Quinone-based Redox Flow Battery Systems

1.3.2 Viologen Based Redox Flow Batteries

Viologen-based redox flow systems, benefit from the redox-active properties of the viologen molecule. **3a** shown below in Figure 13 is the most common type used in these systems. As the image suggests only a single electron reduction occurs in most scenarios, this is due to the once a second reduction is carried out the molecule becomes insoluble in water.

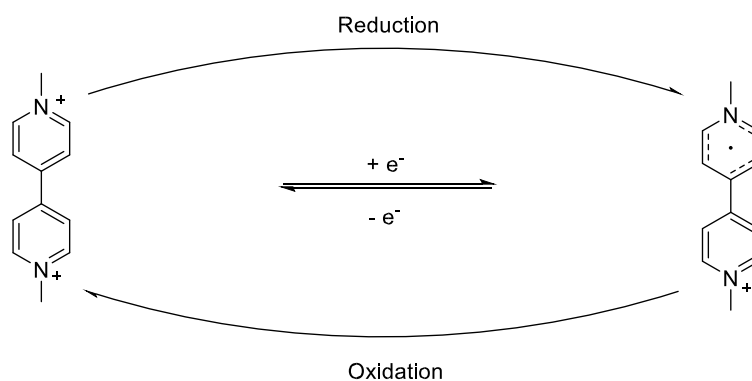


Figure 13 - Redox Pathway of 3a

In a paper published in 2016, an organic battery system utilising **3a** as catholyte and **4b** as the anolyte. This paper also put forward two additional viologen molecules: **3b** and **3c**. The latter three of these molecules are shown below in Figure 14.

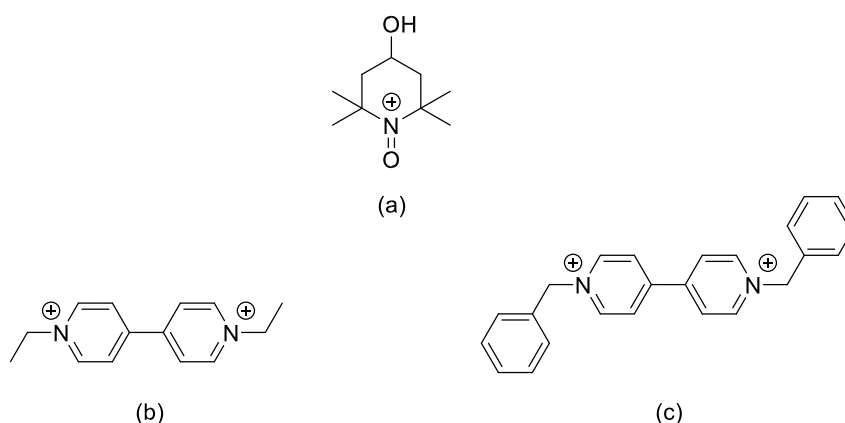


Figure 14 - (a) Structure of 4b, (b) Structure of 3b, (c) Structure of 3c

Out of these three viologen derivatives, MV was found to have the most potential going forward for battery testing due to the low solubility of both **3b** and **3c** (1.5 M and 4×10^{-2} M) respectively when compared to that of **3a** (3.0 M) in aqueous media. This high solubility was reinforced by **3a** also displaying a high reduction potential of -0.45 V vs. Ag/AgCl. Battery testing of **3a** displayed an energy density of 8.4 WhL^{-1} over 100 cycles. ^[47]

Other examples utilising the approach of molecular assemblies are shown below in Figure 15. These assemblies of the molecule to yield improved energy densities and is presented to form assemblies of up to 13 molecules of **3a**.

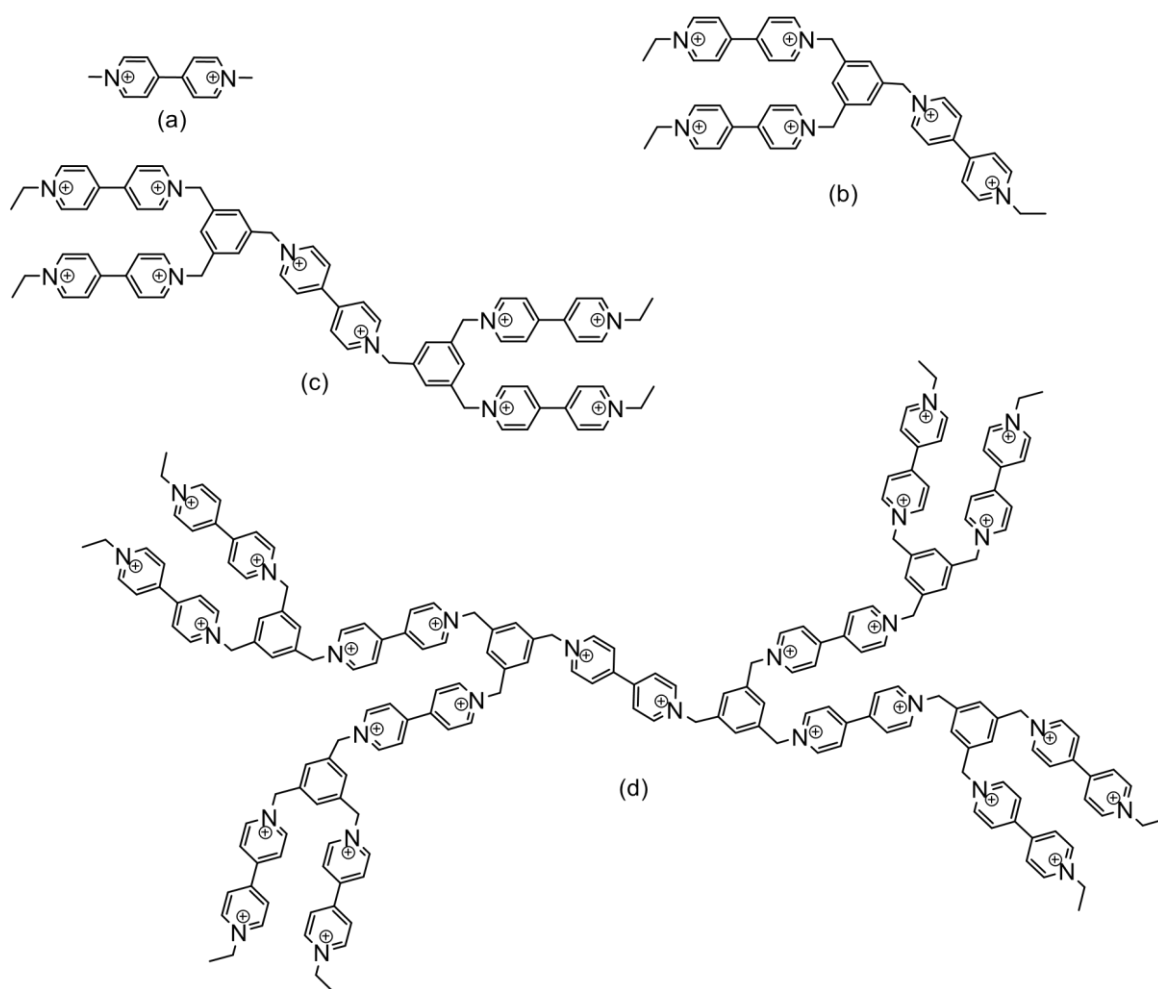


Figure 15 - (a) **3a**, (b) **3d**, (c) **3e**, (d) **3f**^[48]

This approach was reported to have a positive effect on the capacity of the system as it displayed an increased capacity values compared to traditional **3a**-based systems, with values proposed for **3e** and **3f** of 134 and 174 WhL⁻¹ compared to that of the **3a** and **3b** assemblies presenting values of 0.69 and 0.91 WhL⁻¹.^[48]

The above research example further displays the versatility of organic molecules and the effects of this on their uses within flow battery systems – in that the molecule can be designed to overcome specific drawbacks to improve desirable characteristics and thus the molecule's effectiveness within a battery system.

1.3.3 Nitroxyl Based Redox Flow Batteries

Nitroxyl flow batteries, typically derivatives of **4a**-based redox flow batteries rely on the redox active nature of the nitroxyl radical, with the ability for the nitroxyl unit to exist in three different states highlighted below in Figure 16. However, the reduction of **4a** to its anionic form is not typically chemically reversible, as the anion usually decomposes before it can be reoxidised in most conditions. ^[49]

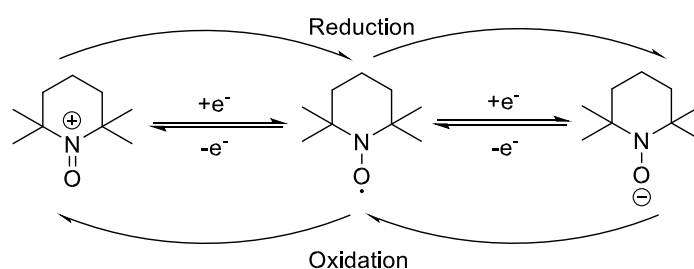


Figure 16 – Redox Pathway of **4a**

A variety of research examples of **4a**-based systems exist to date, with varying complementary redox couples and approaches. Below are three different examples of these types of systems.

An all-organic asymmetrical approach to these system utilising **4c** and **3g**, this system operates at a neutral pH in aqueous conditions, by the movement of chloride ions over an anionic exchange membrane shown below in Figure 17.

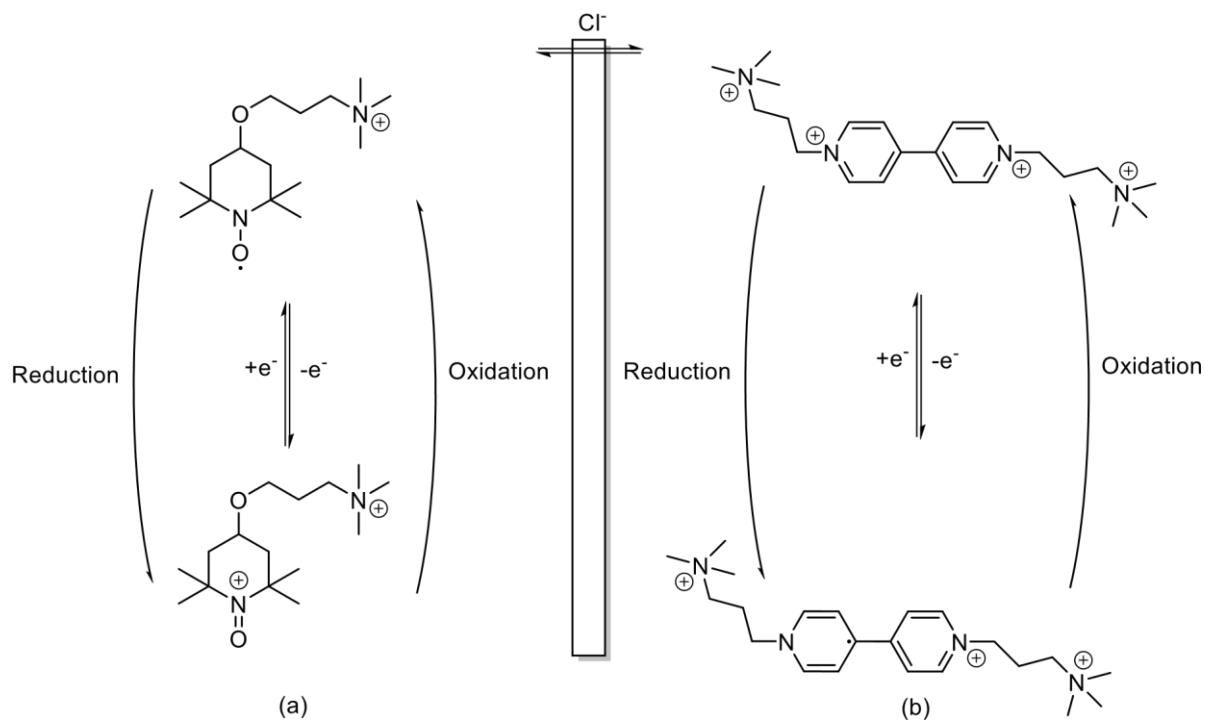


Figure 17 - Schematic Diagram of the **4c** (a) and **3g** (b) cell setup as described in the paragraph above.

This system has a cell voltage of 1.10 V and achieved a capacity retention of 99.993% over a period of 1000 cycles. This paper also reports a total discharge capacity of 25.7 mAh compared to a theoretical capacity of 26.8 mAh (95.9%) however, explains that deviation from the theoretical value was due to a loss of material when transferring the solution/material to and from different containers and electrode overpotentials. ^[50]

Another all-organic symmetrical approach to these systems, illustrated in a paper published in 2016 a combi-molecule approach utilising both the redox couples of **5a** and **4a**. Shown below in Figure 18 is the proposed molecule and its redox pathway.

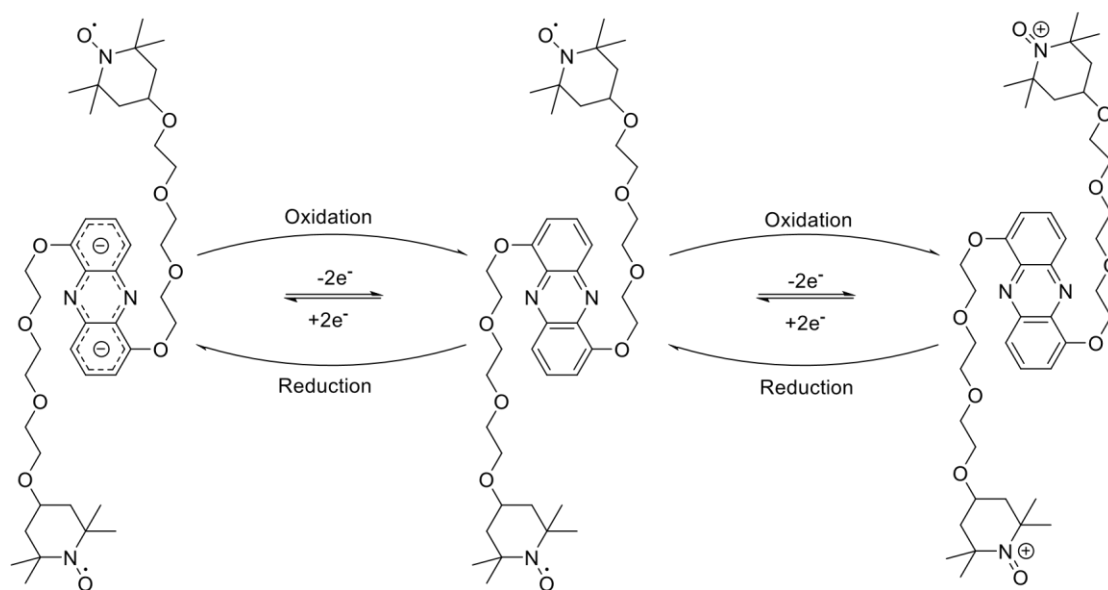


Figure 18 - Redox Pathway of Proposed **4a/5a** Combi-Molecule

The paper goes on to mention that the fully oxidised state is to be used on the cathodic side of the cell whereas, the fully reduced state is to be used on the anodic side - with the 'neutral' state's presence being dependent on whether or not the system is charging or discharging. Results from this system exhibited an energy efficiency of >50%. A long-term experiment was conducted at 4 mAcm^{-2} in which the system was charge and discharged for 1800 cycles resulting in a coulombic efficiency of 98.3% and constant capacity retention. ^[51]

In another publication from 2015, investigating the use of polymers within a flow battery system. Utilising polymeric units in which either included **4a** or **3a** in its structure shown below in Figure 19. Experiments were conducted on both polymers with the **3a** polymer being relatively soluble in water and cyclic voltammetry testing yielding a redox potential at -0.4 V vs. Ag/AgCl alluding to its usability as an anodic material within a battery system. However, the **4a** polymer required a copolymer to be soluble, in which addition of choline was utilised to achieve this increased solubility and a redox potential of 0.72 V was obtained, however testing in a full RFB cell has not been carried out yet. ^[52]

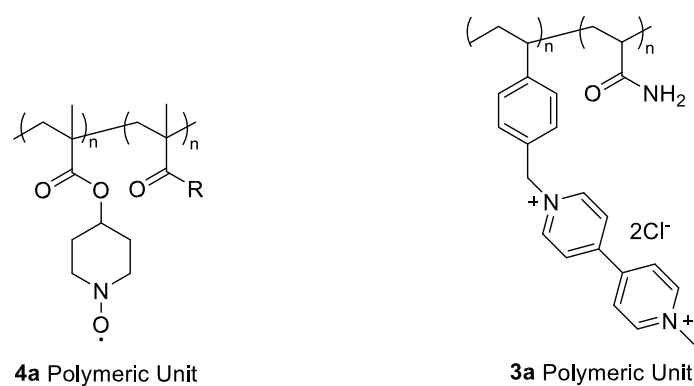


Figure 19 – 4a and 3a Polymeric Units

Limitations of **4a** based RFB systems were demonstrated by Meng et al., who explored the effects of pH on potential side reactions for aqueous systems utilising nitroxyl radicals. This paper found that in acidic environments **4d** disproportionates to form **4b** and **4e** in equivalence (both shown below in Figure 20) before any electrochemical input due to the increased presence of H^+ ions in an acidic solution.

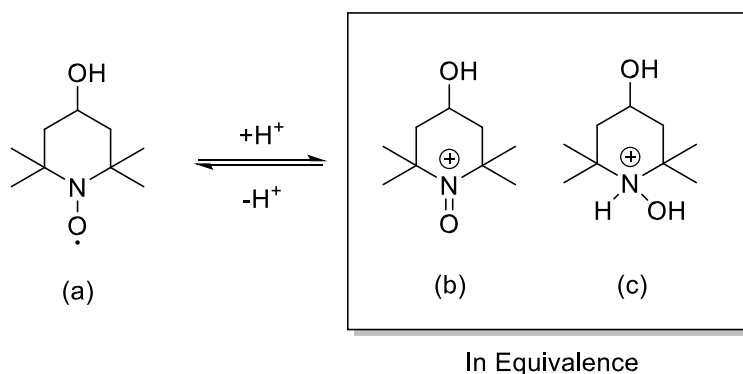


Figure 20 – Pathway of Disproportionation of 4d and Structures of 4d (a), 4b (b) and 4e (c)

This formation of **4b/4e** occurred in even weakly acidic conditions, drawing to the conclusions that if pH deviated from neutral toward acidic in the system; that this formation would cause decreased reversibility. **4b** also was found to react with OH^- ions in basic conditions during cycling which contributed to acidifying the solution.^[53] This indicates that **4a** is only suited to

near-neutral pH environments and that deviation from this to either side of the scale can impact its performance.

1.3.4 Flavin Based Redox Flow Batteries

6a itself is a redox active molecule, its heterocycle **7a** takes the structure of **6a** whilst removing the ribose sugar chain. The further development of that heterocycle can aid to improve the molecule's characteristics such as stability, solubility etc. to best suit its application within a redox flow system.

6a serves a purpose as a redox cofactor in enzymes with its active forms being both **6b** and **6c** (both shown below in Figure 21) acting biologically as hydrogen carriers in the electron transport system.^[54] The molecule can undergo a two-electron redox reaction with the redox potential of **6a** reported to be -0.71 V vs. SCE^[55], making it an area of interest for utilisation as an anolyte in redox flow systems.

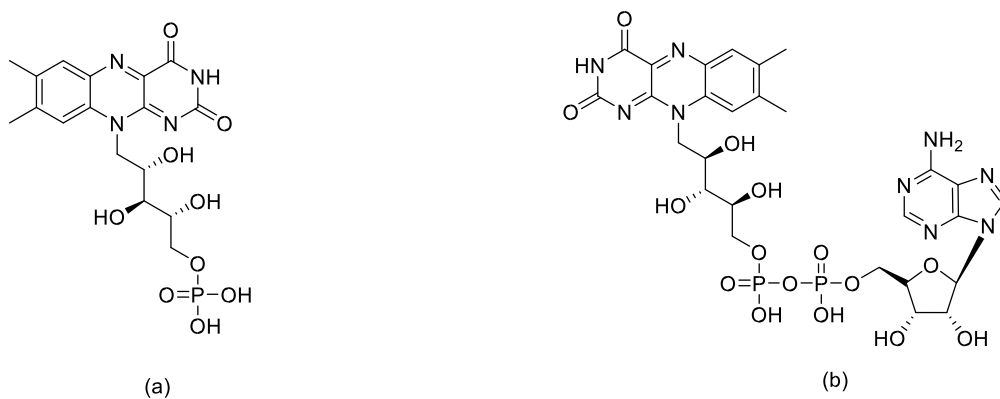


Figure 21 - Structures of **6b** (a) and **6c** (b)

Examples of organic systems utilising **6a**, or its derivatives have yet to be implemented outside of a laboratory setting, although these laboratory examples of these systems have presented

positive characteristics in initial uses within flow battery systems such as high current efficiencies and capacity retention percentages.

In a paper published in 2016 the active form of **6a**, **6b** (pictured above in Figure 20) was utilised in a flow battery system exhibiting a half-cell potential of -0.517 V vs SHE at pH 13. This was coupled with ferrocyanide under these basic conditions, with the half-cell potential of being ferrocyanide being reported at + 0.5 V vs. SHE this would make for a full cell potential of ~1.017 V. This system presented an energy density of 4.83 WhL⁻¹ and a capacity retention of 99% over a period of 100 cycles. This paper also highlights the use of nicotinamide as a hydrotropic agent to further increase the water solubility of **6b**.^[56]

In another paper published in 2016, focusing on **7a** a derivative of **6a**, more specifically a carboxylic acid functionalised variant of **7a**; **7b** shown below in Figure 22.

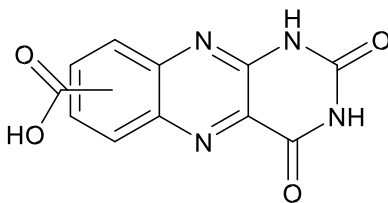


Figure 22 - Structure of 7b

This paper explains that **7b** was coupled with ferrocyanide in a flow cell system, noting a current efficiency exceeding 99% and a capacity retention of ~95% over a period of 400 cycles.^[57] Although these figures only span a 400-cycle lifetime, with both current efficiency and more importantly capacity retention over these 400 cycles remaining above 95%, it demonstrates promise that systems utilising these types of molecules if continued to be developed could offer an organic alternative to current battery solutions.

These systems are not without disadvantages, however; currently flavin-based redox flow batteries are limited in the fact that they can only operate at basic pH. This in general reduces the adaptability of the system and by proxy limits what the flavin can be coupled to – currently only the ferro/ferricyanide couple has been reported.

Chapter 2: Aims

The main aims of the research outlined in the subsequent sections, can fundamentally be broken down into three main categories:

- 1) To successfully synthesise a novel organic molecule for use within a Redox Flow Battery.
- 2) To prove the molecules effectiveness and adaptability within Flow Battery Systems via a range of cyclic voltammetry analyses under different conditions.
- 3) To identify and isolate the ideal conditions for the use of the molecule in these systems.

To achieve the first of these three aims, the molecule would have to strive to abide by the principles of green chemistry and ultimately be synthesised from organic constituents. As a caveat to being an organic molecule, the synthesis of which would have to be straightforward and easily reproduceable, with as few steps in the synthesis and purification as possible to allow for subsequent synthetic attempts.

The second of these aims relies heavily on the successful synthesis and purification of a redox-active organic molecule to be suitable for analysis via cyclic voltammetry and for use in a redox flow system. The ideal outcome of achieving this aim would see the molecule be stable under the operating conditions of the battery and show signs of longevity when operating within a flow battery system. Longevity of which includes little to no capacity fade between charging and discharging cycles.

The final aim again relies on the initial testing of the molecule within a redox flow system – this aim will ultimately determine the molecules flexibility to be used within different conditions within a system and reveal different potential couplings for various molecules that could be used in conjunction with the molecule that is synthesised.

Chapter 3: Results and Discussion

3.1 – Nitroxyl-based Molecules

Currently nitroxyl RFBs inclusive of the nitroxyl radical are typically limited to derivatives of **4a**. This is limiting because the molecule is only stable, with reversible electrochemistry, at neutral pH. ^[53] The possibility of exploring the use of the nitroxyl radical for use in flow battery systems outside of its inclusion in **4a**, could offer alternative products that possess greater stability, tunability and versatility.

Therefore, the initial focus of this report investigates molecules that included the nitroxyl radical, one of these; **8a** shown below in Figure 23 was attempted to be synthesised as a basis to explore the possibilities of using different molecules inclusive of the nitroxyl radical within flow battery systems.

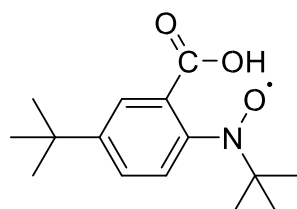


Figure 24 – Structure of 8a

These types of systems offer the same benefits that are inherent of being an organic system as previously discussed. By inserting the nitroxyl radical into various molecules, with the option for further functionalisation – this has the potential to be more electronically tuneable than TEMPO. This expanded versatility allows for the molecule to be consistently adapted to suit its requirement in a system. A generic variety displaying the position of the R-groups on these molecules is shown below in Figure 24.

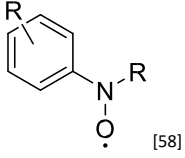
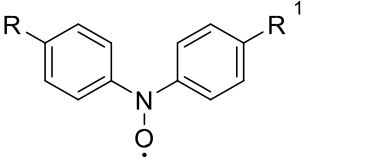
Molecule	Operating Conditions (Base/Neutral/Acid)
	Dependent on R-Group
	Dependent on R-Group/s

Figure 24 - Table showing two different types of Nitroxyl-based Molecules of Interest

The latter of these two molecules in Figure 24 above, shows the nitroxyl surrounded by two aryl rings. This initial structure has been successfully synthesised with $R/R^1 = tBu$ and $R/R^1 = CF_3$ [58], with the former being a possible candidate for testing as an ambipolar redox-active material [59] meaning that it can exist in both exist in its anionic and cationic form, with the radical form being an intermediate between these two forms.

Although these systems come with a variety of advantages, they are not without disadvantages. Some of these molecules can be difficult to synthesise and currently often rely on expensive reagents during synthesis. At present, synthesis and electroanalysis of a water-soluble aryl nitroxyl has not been done and these systems are currently limited to operation within other conditions.

The overall goal of this project was to successfully synthesise a redox-active organic molecule, which could then be utilised in a flow battery system. Firstly, the molecule synthesised would have to facilitate this redox reaction with a high degree of reversibility. Secondly, the molecule/s cheap to produce; a main drive for redox flow battery research is to provide an

electronically competitive but cheap alternative to current battery technologies. Thirdly, the molecule/s need to be soluble in water. This goes hand in hand with being an already cheap alternative to inorganic flow systems in that they utilise these cheap organic molecules, the extended ability to utilise water as a solvent within these systems further drives the price down and eliminates the need for any organic solvents that may be hazardous to use within the system.

Following these three aims along with the checklist of prerequisites about the properties and behaviour of the molecule, and now knowing the specific limitations of other nitroxyl-based systems specifically **4a** – the proposed synthesis of **8a** – shown below in Figure 26b looked promising and adhered to these prerequisites.^[60] This initial proposed synthesis, based on a literature synthesis of **8a** consisted of five-stage stages shown below in Figure 25 coupled with an extra step for the formation of the nitroxyl radical.

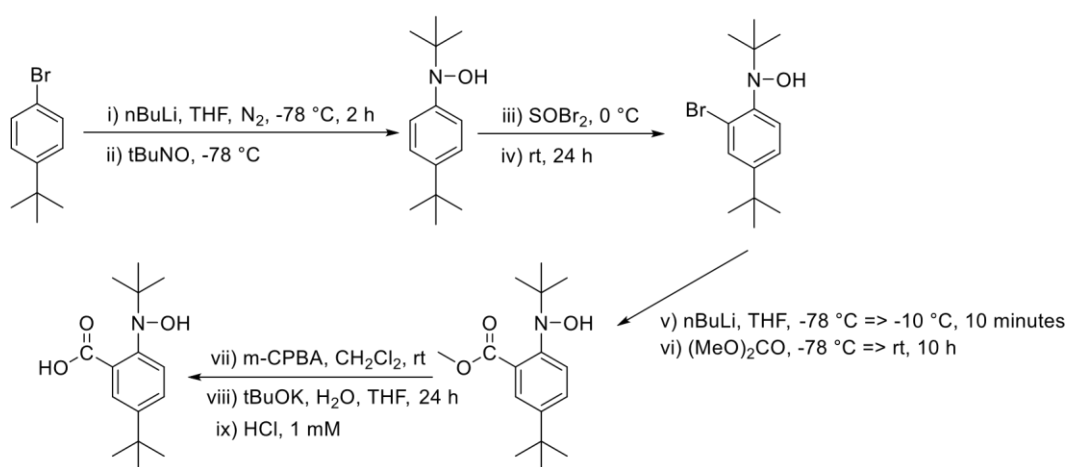


Figure 25 - Complete Reaction Pathway to synthesis **8a**

To facilitate the initial synthesis of **8a** shown below in Figure 27b, **9a** shown below in Figure 26a was first to be synthesised.

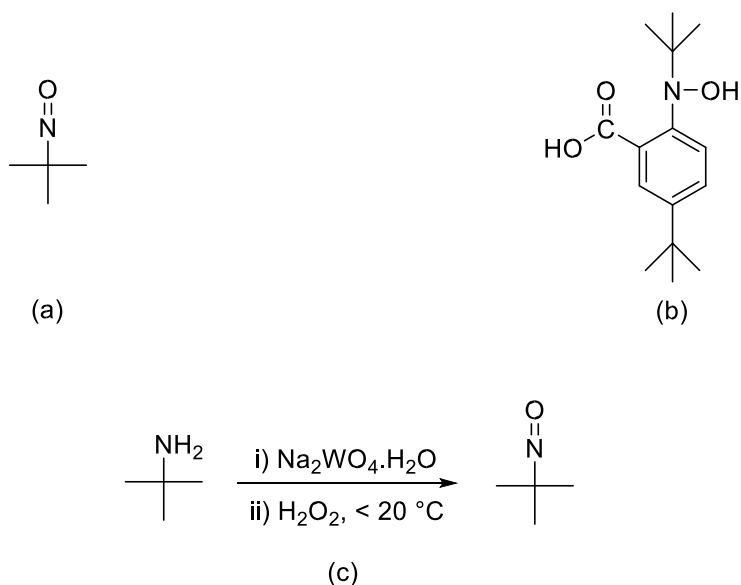
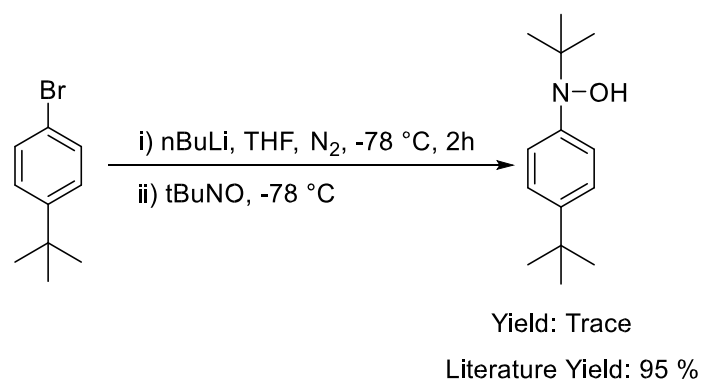


Figure 26 - Structures of **9a** (a) and **8a** (b) and Reaction Pathway for Synthesis of **9a** (c)

The main synthesis of **9a** was as previously stated relatively simple as shown above in Figure 26c. However, the isolation of **9a** in its monomeric form proved more difficult than anticipated, with the process requiring an $>80\text{ }^\circ\text{C}$ distillation to extract the monomer. Initially, distillation was noted to be around $80\text{ }^\circ\text{C}$ ^[61] however after prolonged heating at this temperature no distillate was observed. Slowly ramping the temperature up until a distillate was observed running off ($\sim 110\text{ }^\circ\text{C}$) solved this issue, however as noted in the source publication the distillate needed immediate cooling to prevent excess heat of crystallisation causing the product to evaporate. Co-distillation of water was also a challenge in product isolation. In later attempts at this synthesis, it was found that if the resultant reaction mixture was cooled for a long period of time ($>48\text{ hrs}$) large needle-like crystals of the monomer would form. These crystals presented themselves as a separate layer on the top of the aqueous layer in the vessel. These crystals could be picked out of the solution and were largely absent of H_2O when left to dry in air.

The successful synthesis of the **9a** monomer then provided the means to be able to carry out the synthesis of **8a** shown above in Figure 27b. The first step of this synthesis involved the lithium-halogen exchange between 4-bromo-tertbutylbenzene and nBuLi shown below in Figure 27.



*Figure 27 - Initial Step of **8a** Reaction Pathway*

Standard air-free/Schlenk techniques were used in all lithiation reactions. However, the effectiveness of these measures and the effect of air influx into the reaction could be the contributing factor to the low yield and purity of this reaction. In addition, it is possible that the internal temperature of the reaction mixture could have risen above -78 °C at some point during lithiation and thus caused side reactions to occur. The second step of the reaction shown above in Figure 27 utilised **9a** to then quench this reaction.

Due to the low yield and purity of the nitroxyl product as a result, an alternative reaction pathway was attempted by the formation of a Grignard reagent as opposed to the lithium-halogen exchange method used previously shown below in Figure 28.

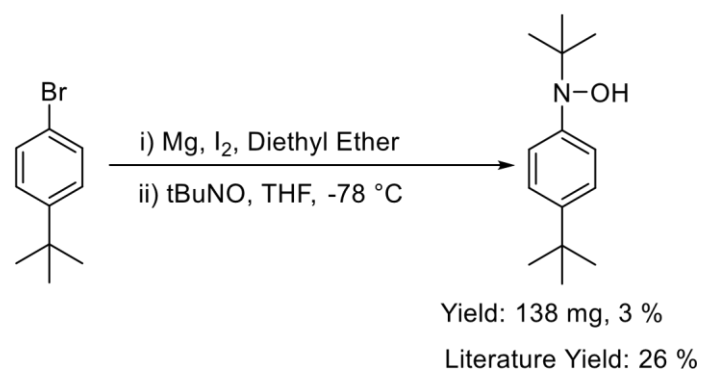


Figure 28 - Reaction Pathway of 8a Utilising a Grignard Reagent

This reaction pathway came offered a better theoretical yield than utilising nBuLi, which would hopefully a larger amount of product to continue synthetic efforts with. Column chromatography was utilised which then yielded a red oil. The product from this reaction was then used to attempt the second of the 6-step reaction, shown in Figure 29a. This involved the utilisation of SOBr₂ and Et₃N to brominate a position on the aryl ring which would later then be substituted for a carboxylic acid via method of hetero-cope rearrangement ^[62] – a mechanism for this reaction can also seen below in Figure 29b.

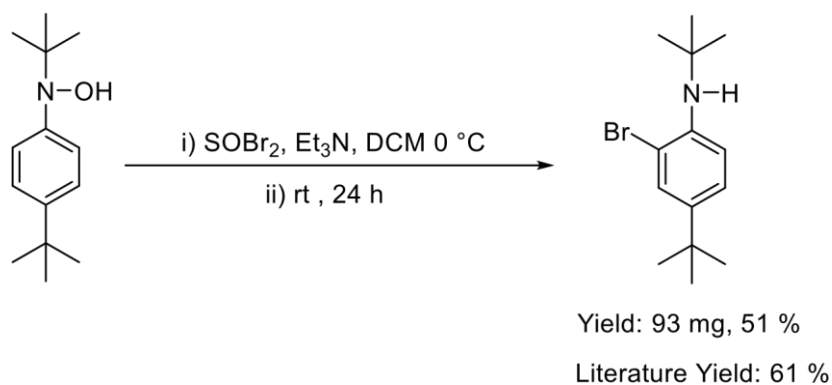


Figure 29a - Step 2 of **8a** Reaction Pathway

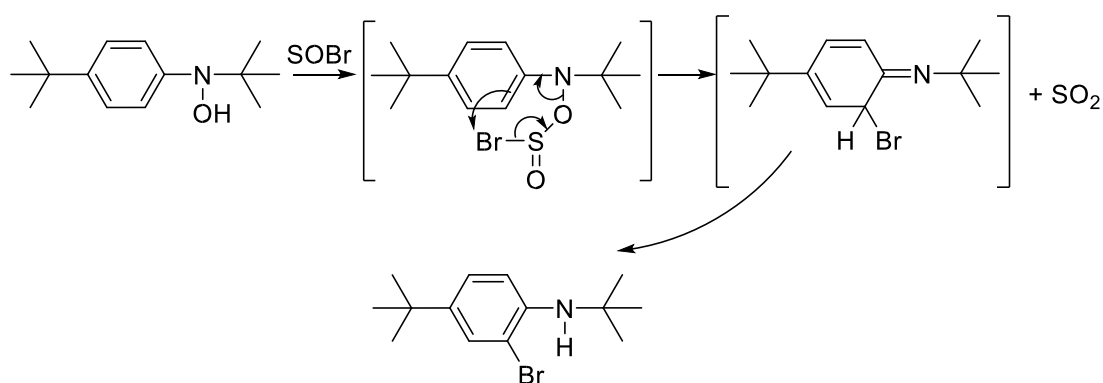


Figure 29b - Mechanism of Step 2a of **8a** Reaction Pathway^[62]

Although this reaction seemingly worked, the yield that was provided (93 mg) was deemed too little to continue efforts in synthesising **8a**.

Due to the low yields within each step for both synthetic methods utilised in the attempt to synthesise **8a** with an end yield of 93 mg at step two out of 6, a decision was made to further explore alternate methods in which a different nitroxyl based molecule could be achieved.

The focus was then switched to a second target molecule, **10a** shown below in Figure 30, due to this reaction presenting fewer synthetic steps than the one attempted previously.

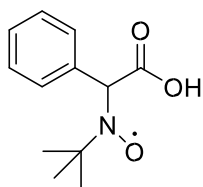


Figure 30 - Structure of **10a**

Again, much like the synthesis of **8a** – n-BuLi is added to the reaction at -10 °C under inert conditions, followed by the addition of **9a** and finally opening the reaction mixture to air.

(shown below in Figure 31)

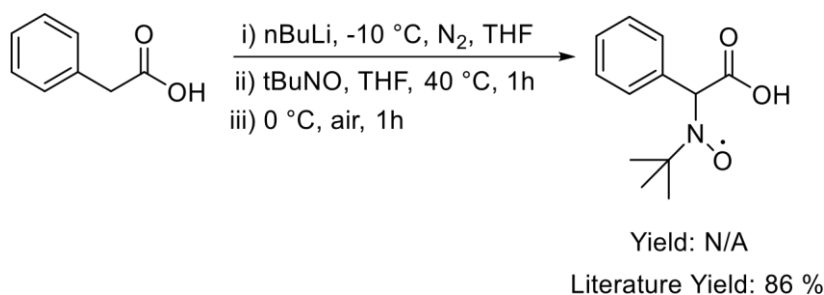


Figure 31 - Reaction Pathway to Synthesis **10a**

Initial analysis of this molecule by method of $^1\text{H-NMR}$ was carried out, with the expectation of observing broad peaks spectrum indicative of the presence of a radical. This however, was not the case and no evidence of paramagnetic material was presented in the spectrum, instead multiple cluttered sharp signals between 7-8 ppm and 2-1 ppm were seen. A second $^1\text{H-NMR}$ experiment was conducted, but this time utilising phenylhydrazine to reduce the possibly present nitroxyl radical and yield more conclusive NMR data, this spectrum whilst still including the multiple sharp signals between 7-8 ppm and 2-1 ppm introduced a broad peak at 4.15 ppm which if at all would have been expected to be seen in the former of the two analyses corresponding to the presence of the nitroxyl radical, so the fact that it is observed during the latter instead would indicate that the presence of the nitroxyl radical could not be determined from NMR. Taking the data from the first NMR spectrum and the indication that the nitroxyl

radical was not present in this sample, further analysis via cyclic voltammetry was conducted to try and confirm and reinforce this data.

Displayed in Figure 32 below, is the cyclic voltammetry data for **10a** conducted in a 15 mL 0.1 M solution of NaOH using 15 mg (0.67 mmol) of sample for a concentration of 45 mM. As described this experiment is run in alkaline conditions, in order to facilitate aqueous solubility of **10a** as a carboxylate salt. This data as the figure suggests is inconclusive and suggests negligible redox activity.

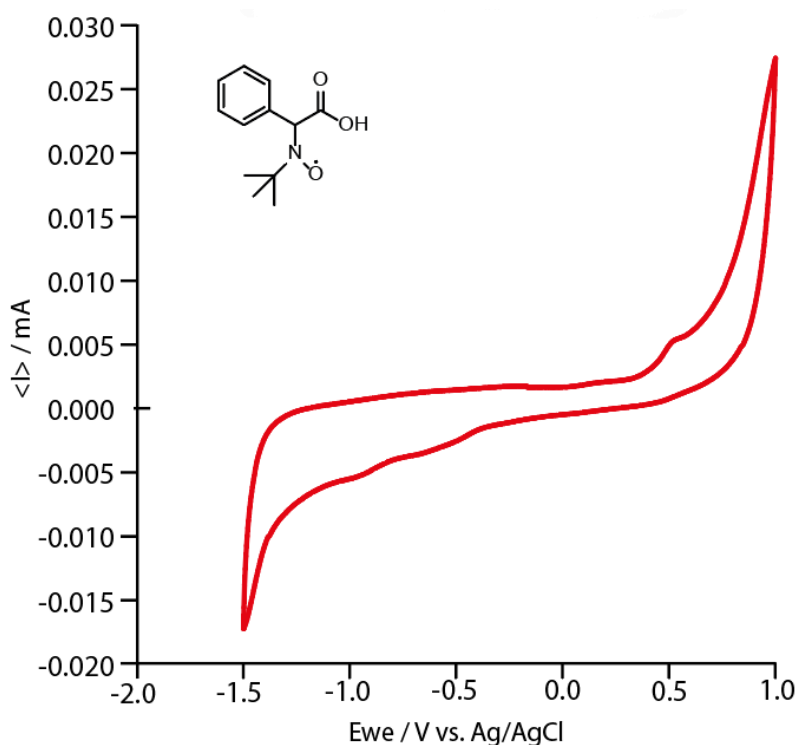


Figure 32 – 10a CV Current vs. Voltage against a Ag/AgCl Reference Electrode for 10a in 0.1 M NaOH at 100 mV - Extended Information: Cyclic Voltammetry conducted using Standard Operating Procedures as listed in Experimental Chapter.

This is explained by the absence of any reduction and oxidation events in the graph, and that the two apparent oxidation and reduction events at -1.5 V and +0.8 V is linked to the

electrochemical window of the solvent. There is a minor peak around +0.5 V in this data which could be linked to an oxidative event, however, there is no observable reduction to counter this. External research conducted on a different molecule inclusive of the nitroxyl radical; **4d** illustrates that at pH 12.6 reversibility of the molecule ceases after the initial oxidation event as in strongly basic conditions **4b** can readily react with OH⁻ ions to form **4d**.^[51] If the same effect that occurs with **4d** at pH 12.6 is happening in this instance then it would explain the redox behaviour seen if **10a** was indeed actually present. Due to the unfavourable behaviour of **10a** during the analysis via cyclic voltammetry the decision to abandon research efforts into this molecule was taken.

3.2 – Flavin-based Molecules

Alloxazine based systems have been published to achieve low-capacity depreciation per cycle^[34] but are currently limited to what conditions they can be utilised in; either operating in neutral or basic pHs. As well as current molecules being synthesised only from synthetic precursors. **11a**, is a molecule that can be synthesised from its natural precursor riboflavin by elimination of the ribose sugar chain and/or synthesised from the two synthetic fragments: 4,5-dimethyl-1,2-phenylenediamine and Alloxan (2,4,5,6-Tetraoxypyrimidine) shown in Figure 33 below.

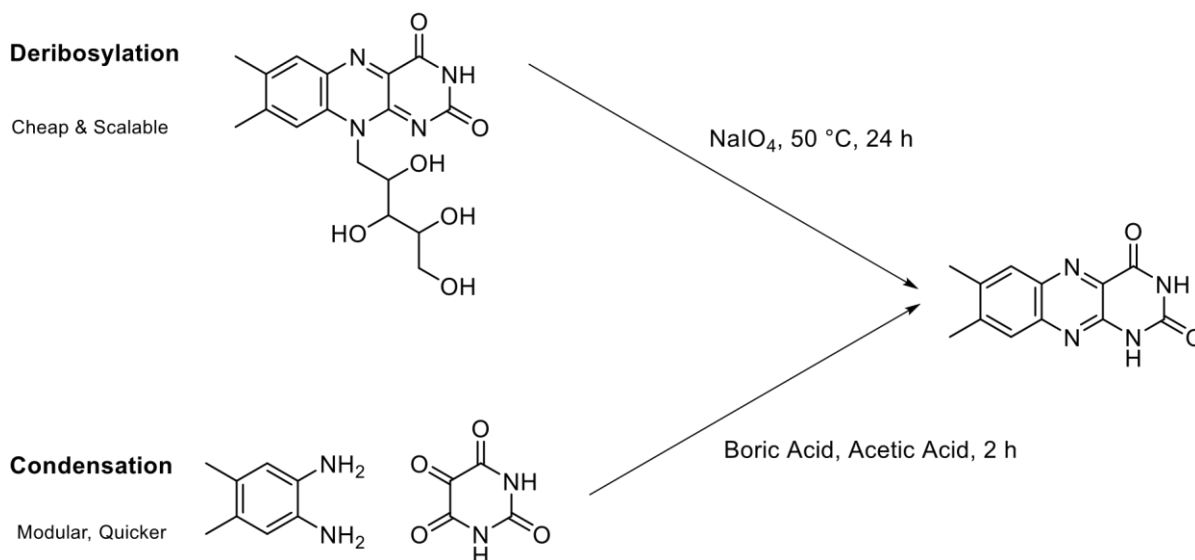


Figure 33 - Two Synthetic Pathways for the Synthesis of 11a and their Individual Advantages

However, **11a** is only soluble in strongly basic conditions and not in water, which for application within aqueous systems is far from ideal as it hinders how adaptable this molecule can be. As an organic molecule **11a** has the versatility of undergoing functionalisation to alter the properties of the molecule and make it best suited for these applications.

The latter of the reaction pathways shown in Figure 30 offered a faster of a reaction and due to time constraints of the project, was selected as the best pathway to produce **11a** for RFB testing purposes. The overall synthesis of **11a** proved to be facile, with a simple one pot reaction that required stirring/heating for two hours and then washing with solvents after this time. To address issue with water solubility two moieties: Trimethylamines and Sulfonates tethered with alkyl linkers were considered for this purpose as they could be easily added to the two imides (position 11 & 13, shown below in Figure 34) atoms via a S_N2-type reaction.

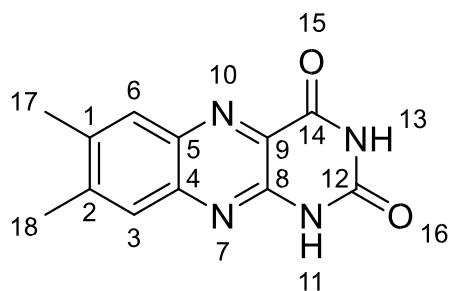


Figure 34 - Atom Numbered Structure of **11a**

These two different functional groups offered different charges, to potentially give the capability of utilising each of the different molecules shown below in Figure 35 in varying conditions and/or with different membranes.

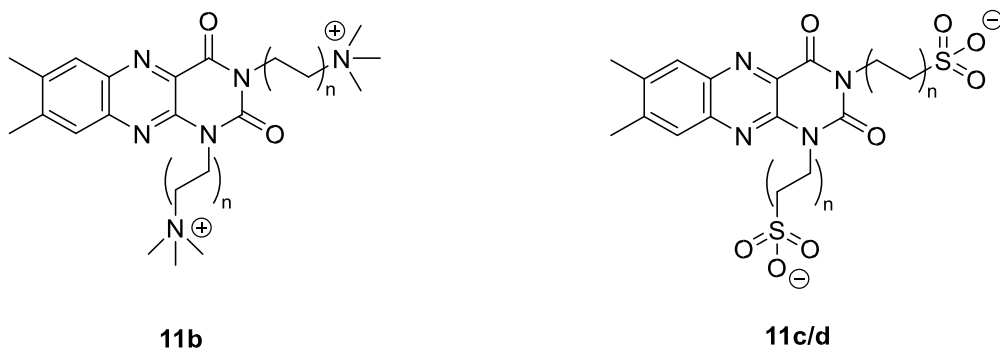


Figure 35 - Structures of **11b** and **11c/d**

These two reactions sometimes halted before complete disubstitution was observed via ^1H NMR, this necessitated longer reaction times, the addition of multiple portions of the respective electrophile and even the input of more energy into the system (via heating) to drive the reaction to completion as shown below in Figure 36

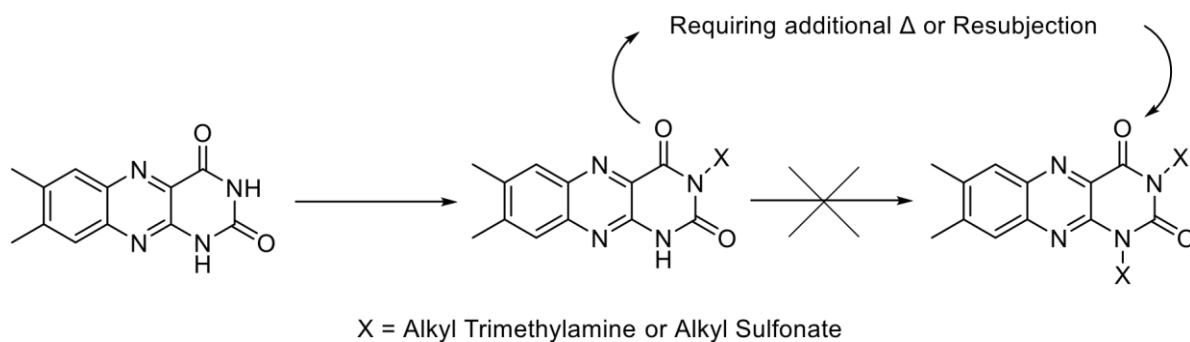


Figure 36 - Illustration depicting Monosubstitution of **11a**.

For the sulfonate pathways, two different chain lengths were chosen as a start point: butyl and propyl sulfonate, utilising 1,4-butane sultone and 1,3-propane sultone, shown below in Figures 37 & 38, respectively.

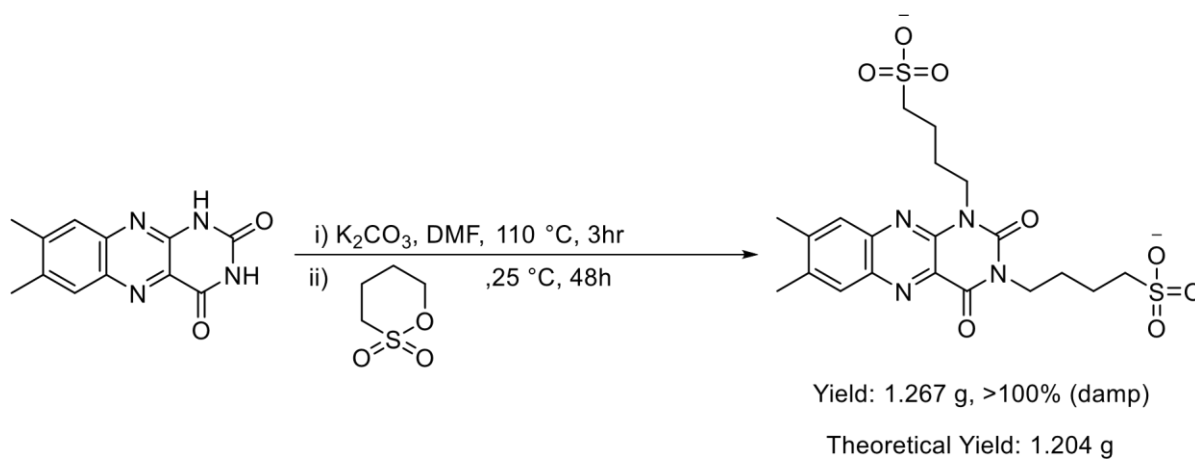


Figure 37 - Reaction Pathway for substitution of 1,4-butane sultone to **11a**

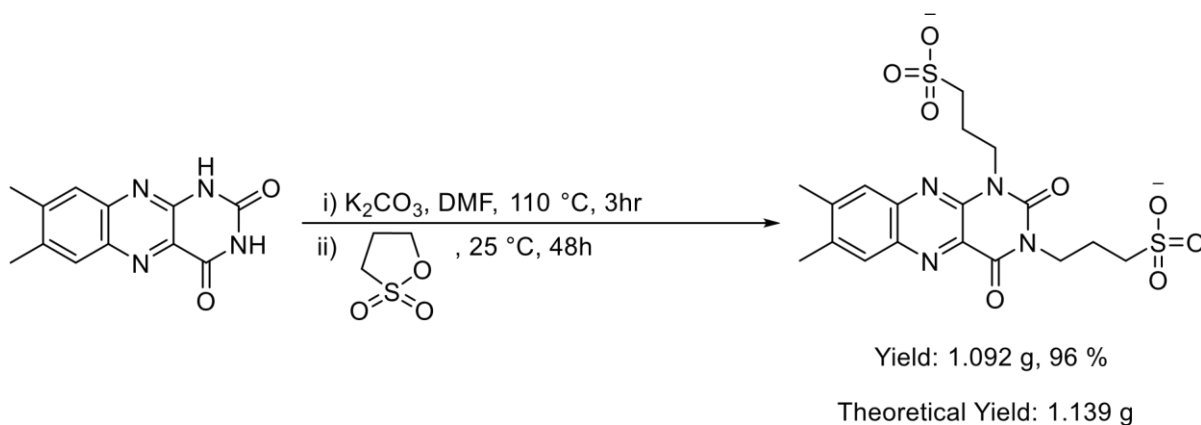


Figure 38 - Reaction Pathway for substitution of 1,4-propane sultone to **11a**

During these two pathways, it became apparent that the reaction between **11a** and 1,4-butane sultone was slower than its propyl counterpart, with the reaction not progressing to completion despite being subjected to the same conditions as the **11a**/1,4-propane sultone reaction. This may be due to the shorter of the sultones being more electrophilic compared its longer chain counterpart. This disparity between the two reactions and the knowledge that the shorter chained of the two molecules would innately be more soluble in water contributed to **11d** being the focus of further synthetic efforts.

During the numerous syntheses of **11d**, various results were observed, with some reactions progressing to completion after a reaction time of 48 hours and no external heating or resubjection – others, however, did require gentle heating and on one occasion multiple further additions of 1,3-propane sultone to complete shown above in Figure 33. The requirement for these different conditions for the progress of the same reaction in different instances could be an effect of the scale of which the reaction was carried out. At a larger scale it is possible for different factors to affect the time that the reaction takes to reach completion, such as: the mixing rate of the reaction vessel, if kept constant between a small and large scale reaction this will increase reaction time. Due to when scaling up a reaction, factors such as the reaction

kinetics of the larger scale reaction needed to be considered. With more material in the reaction vessel, this required stirring at higher speeds and in most cases required more energy input into the system via heating to achieve total completion of the higher mass of reactants.

The first of the flavin series to be synthesised in this project, **11b**. Presented in Figure 39 (below) is the data for **11b** run in a 15 mL 0.1 M solution of NaCl with 15 mg of sample for a concentration of 24 mM.

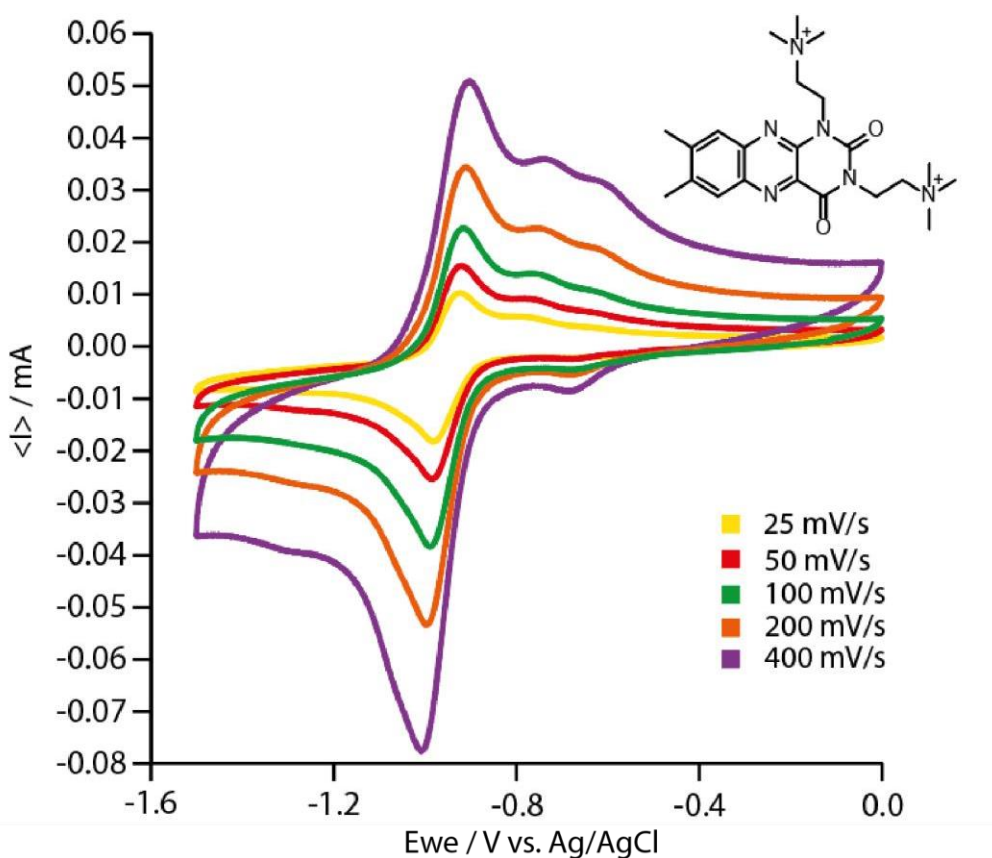


Figure 39 – 11b CV Current vs. Voltage against Ag/AgCl Reference Electrode – 0.1 M NaCl at Varying Scan Rate - Extended Information: Cyclic Voltammetry conducted using Standard Operating Procedures as listed in Experimental chapter.

The data shows a reversible wave that is to be expected from a redox-active organic material, indicated by the alignment of both the reduction and oxidation events with a peak-to-peak separation of 0.176 V and $E_{1/2} = -0.901$ V at 100 mV/s. However, within this data it can also be seen that there is a satellite redox signal occurring toward the more positive side of both of these events. This satellite event is evidence of another reduction occurring within the sample, either by means of an impurity, a second reduction on the target molecule itself or deposition of the molecule onto the electrode.

Figure 40 below show the cyclic voltammetry data acquired for **11d** at 20 mM in a 0.1 M solution of NaCl (pH 7) across varying scan rates. The data from this analysis shows singular reduction and oxidation events in each of the different scan rates, as well as following the typical Nernstian shape. This graph shape is indicative of what is to be expected when analysing a redox-active molecule by method of cyclic voltammetry as the symmetrical nature of both reductive and oxidative events displays the reversible nature of the redox reaction within the molecule. This figure also displays a peak-to-peak separation of 0.097 V and an $E_{1/2} = -0.893$ V vs Ag/AgCl at 100 mV/s. The recorded peak-to-peak separation of 0.097 V at 100 mV/s is larger than the expected <59 mV for an ideal reversible system and is more concurrent with quasi-reversible systems in where electron transfer is slower.

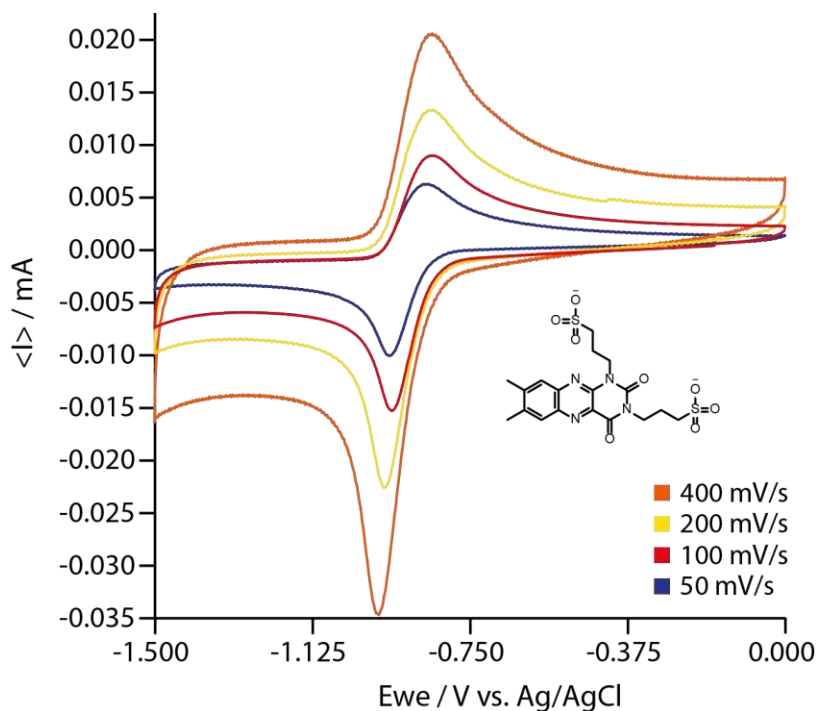


Figure 40 –11d CV Current vs. Voltage in 0.1 M NaCl at pH 7 against a Ag/AgCl Reference Electrode - Extended Information: Cyclic Voltammetry conducted using Standard Operating Procedures as listed in Experimental chapter.

To then explore the versatility of **11d** within acidic conditions, 20 mM of **11d** was dissolved in a 0.1 M solution of H₂SO₄ (pH 1) across varying scan rates shown in Figure 41 below. It can be seen compared to the data in Figure 40, that the redox potentials for each scan rate are more positive when the experiment is conducted in acidic conditions. The figure shows a peak-to-peak separation of 0.039 V which is indicative of two-electron transfer (<59 mV) and an $E_{1/2} = -0.728$ V vs Ag/AgCl at 100 mV/s. Comparing this peak separation for acidic conditions to those conducted in neutral conditions, it is seen that the peak separation is smaller and more constant with a difference of 2 mV between the $E_{1/2}$ values for readings at 25 mV/s and 200 mV/s (33 mV and 35 mV respectively) when conducted in acidic conditions thus it appears that the molecule shows a higher degree of electrochemical reversibility.

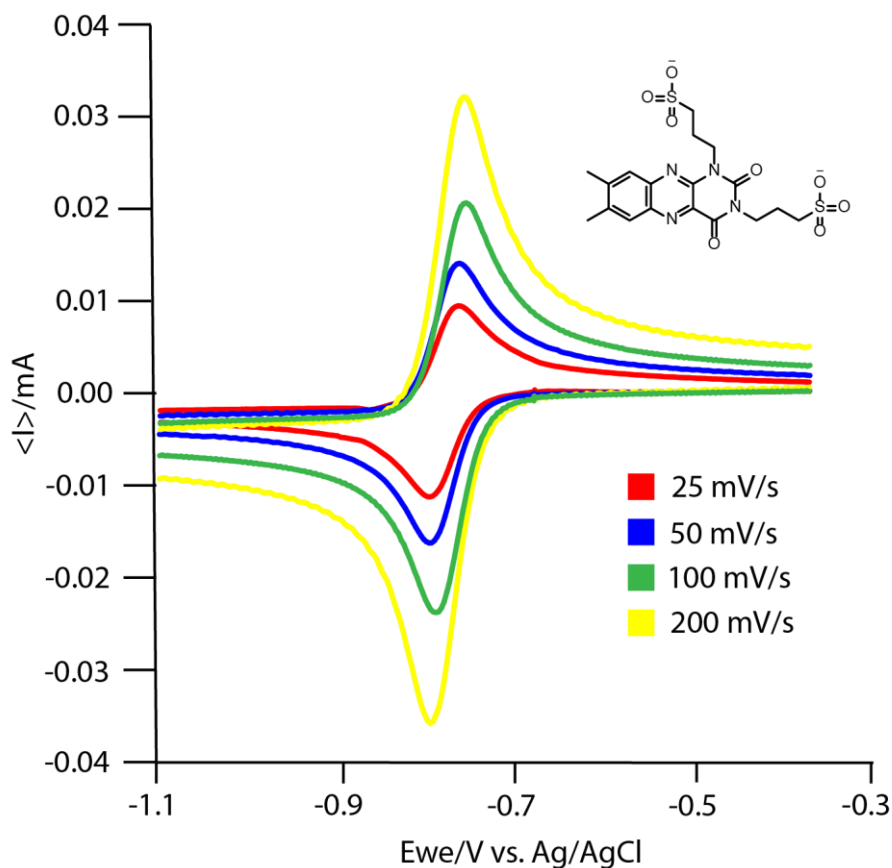


Figure 41 – 11d CV Current vs. Voltage in H₂SO₄ against an Ag/AgCl Reference Electrode at Varying Scan Rates - Extended Information: Cyclic Voltammetry conducted using Standard Operating Procedures as listed in Experimental chapter.

To take this further Figure 42 below, the data shows a 20 mM sample of **11d** at varying pH utilising a phosphate buffer to regulate pH across the range of pH 2-6, acidifying with 1 M HCl. From this data it can be seen that the effect of a more acidic pH and therefore a higher concentration of H⁺ in the system shifts the cell voltage to a more positive state ranging from -0.972 V at pH 6 to -0.850 V at pH 2, with an overall half-cell voltage difference of 0.122 V.

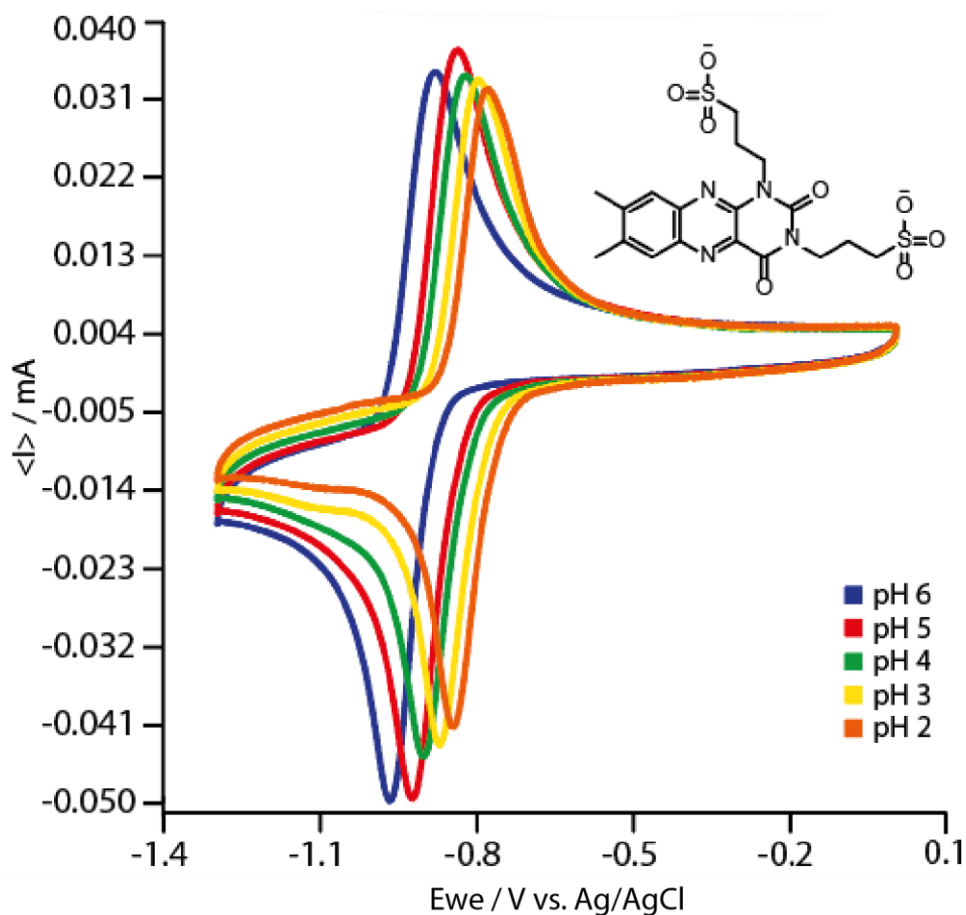


Figure 42 – **11d** varying Buffered pH CV Current vs. Voltage against an Ag/AgCl Reference Electrode - Extended Information: Cyclic Voltammetry conducted using Standard Operating Procedures as listed in Experimental chapter.

Below in Figure 43, the graph depicts the effects of pH on $E_{1/2}$, plotting this data provides insight into how many electrons and protons are being transferred based on a movement of 60 mV/pH if two electrons and two protons are being transferred as expected.^[63] However, the data in Figure 43 suggests that at most $E_{1/2}$ changed by 44 mV between pH 1 and 2. Although this value strays from literature value of 30 mV/pH for each electron involved in the transfer, the CV data still showed promise in utilising **11d** in a flow system. However, work done on this molecule succussing this thesis has produced results more in accordance with the literature value of 30 mV/pH.^[64] Therefore, the disparity between the experimental results seen in Figure

43 and literature result, could potentially be explained by quality or preparation of the reference or working electrodes.

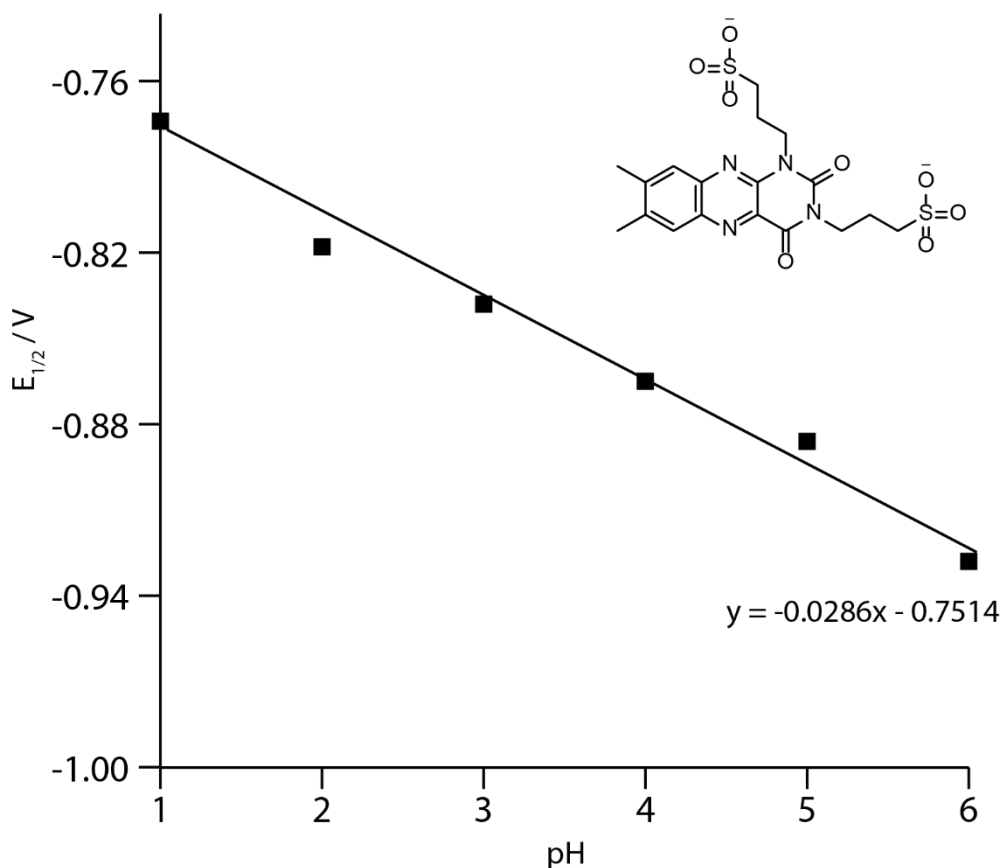
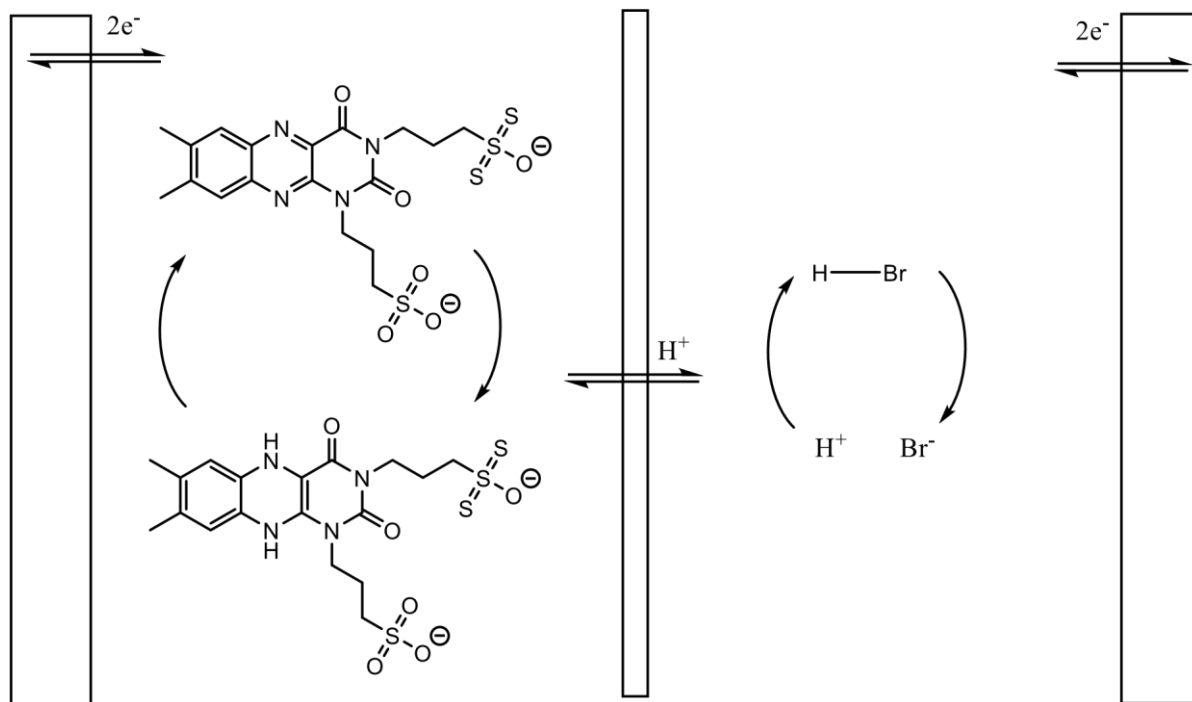


Figure 43 - A Graph to show the effects of pH on E_{1/2} for **11d**

With promising results from both neutral pH and acidic pH cyclic voltammetry experiments using **11d**, a range of flow battery experiments were planned and executed. In the bulk of these experiments the redox couple of HBr/Br₂ was selected, this is due to the knowledge of this being a working couple which has shown to work in literature including both inorganic and organic flow battery systems, but more specifically for use with anthraquinone-based systems.

[57]

Attempting to replicate the successful systems presented in literature that utilise this couple, but instead replacing the anthraquinone with **11d** this provided a good starting point to develop this system. A generalised schematic diagram of this battery set up is shown below in Figure 44.



*Figure 44 - Schematic Diagram of **11d** || HBr/Br₂ Battery Setup with Bromine being Produced in the Right Side of the Cell and Electron Transfer occurring between the Molecules and Electrodes respectively.*

Figure 45 below illustrates the cell voltage vs. capacity for a 100 mM solution of **11d** in 0.1 M H₂SO₄ acting as the anolyte coupled with a HBr/Br₂ catholyte. As seen in the data, the capacity that the battery charges to is almost directly related to the current at which it is charged at. A higher current in these experiments caused the battery to high the set voltage limit of 1.8 V a lot sooner than at lower currents, which in turn allowed the battery to charge for a longer period of time and to a higher capacity. It can also be seen that the depth of discharge for each of these data sets run at different currents is around 15-16%, meaning that a lot of charge is being lost or is becoming inaccessible between the charging and discharging cycle.

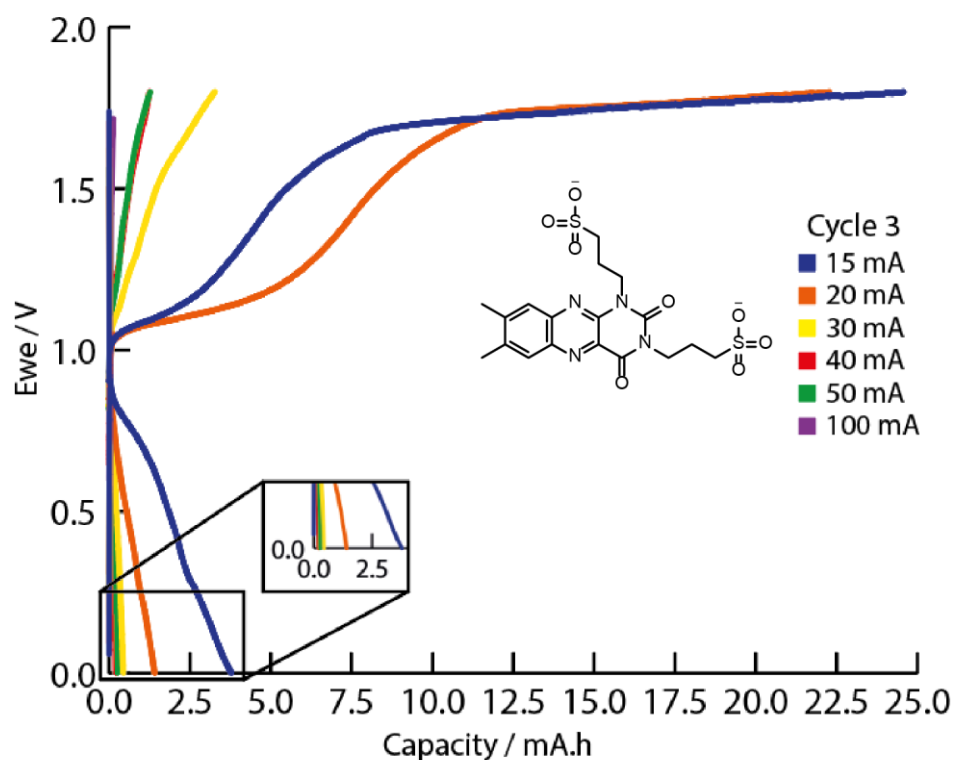


Figure 45 - Cell Voltage vs. Capacity for **11d** coupled with HBr/Br₂ at Varying Current

Further experiments utilising **11d** in flow battery systems were carried out. These experiments differed in which redox couple was paired with **11d** and were aimed at exploring different redox chemistries and the results that they yielded to see if they would have a positive or negative influence on the capacity and current efficiency of the system.

Figure 46 below shows the data yielded from a battery experiment conducted with a 100 mM solution of **11d** in a 0.1 M solution of H₂SO₄ coupled with a 0.1 M HI catholyte. This time run at a charging current of 10 mA and a discharging current of -2.5 mA, these currents were found to be the optimal values for charging and discharging at the concentration used in the battery. The decision to use HI in place of HBr/Br₂ was made as HI was thought to be more reversible and further away from the potential window of H₂O, so this made it an ideal choice to trial as a couple.

This graph shows the data from cycle 10 through 15 for the battery system. Initially cycle 10 charges to a capacity of ~9 mA.h and discharges only ~1 mA.h of this. The next cycle displays a capacity fade of ~56% from cycle 10 to cycle 11, with cycle 11 presenting a charging capacity of ~4 mA.h, again only discharging ~1 mA.h of this. Subsequent cycles exhibit more capacity fade from cycle to cycle, however at a lessened magnitude but discharging capacity remained relatively constant throughout the experiment staying around ~1 mA.h. In this case, I₂ was physically observed to precipitate out of solution, which is most likely the cause of this poor performance.

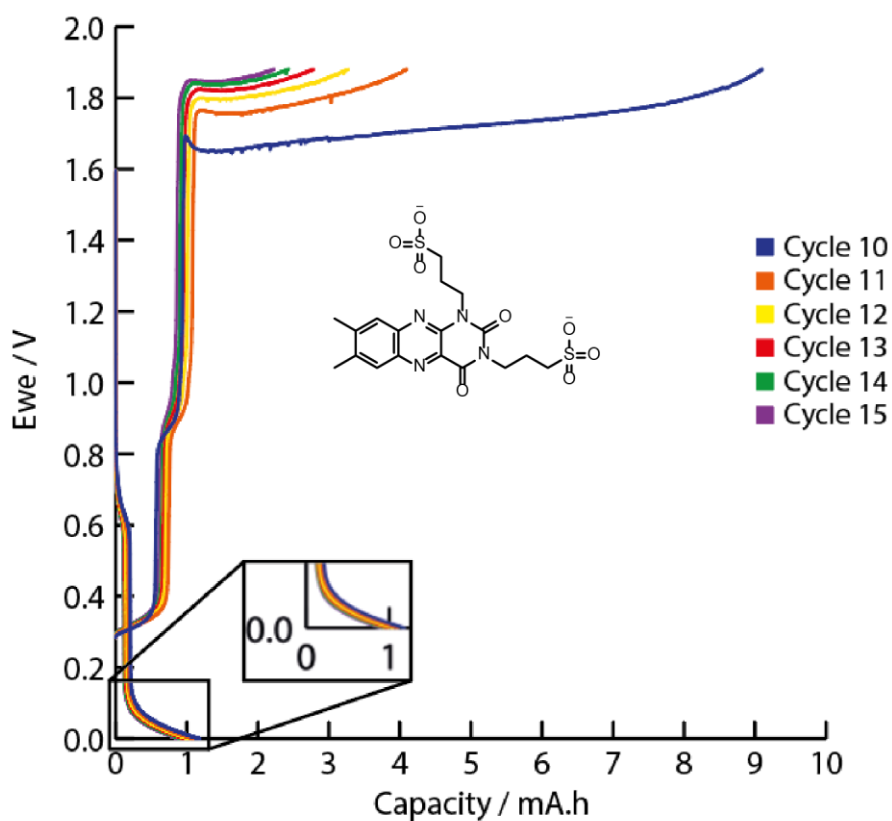


Figure 46 - Cell Voltage vs. Capacity for **11d** coupled with HI/I₂

As a comparative study between **11d** and a known flow cell setup, an experiment was run utilising a 100 mM solution of the quinone, **1a** in 0.1 M H₂SO₄ coupled with a 0.1 M solution of HBr/Br₂.^[43] Figure 47 below illustrates the results from this experiment in which a capacity gate of 11 mA.h was set to prevent the system from ‘overcharging’, this capacity gate was set according to the calculated theoretical capacity of the solution. Along with this capacity gate, charging and discharging current were set at 10 mA and -1 mA, respectively. In this graph it can be seen that all cycles charged to the gate of 11 mA.h however with an observed voltage increase from ~0.90 V to ~0.95 V. It can also be seen that the discharge capacity increases proportionally to the voltage increase, resulting in a maximum discharge capacity of 2.1 mA.h. This disparity between charging and discharging capacity between our experiment and the literature values for these quinone systems unfortunately did not come close to expected values. This could be an indication of limitations of the system at low concentration, or potential limitations of the flow cell setup, such as flow rate inducing mass transport limitations.

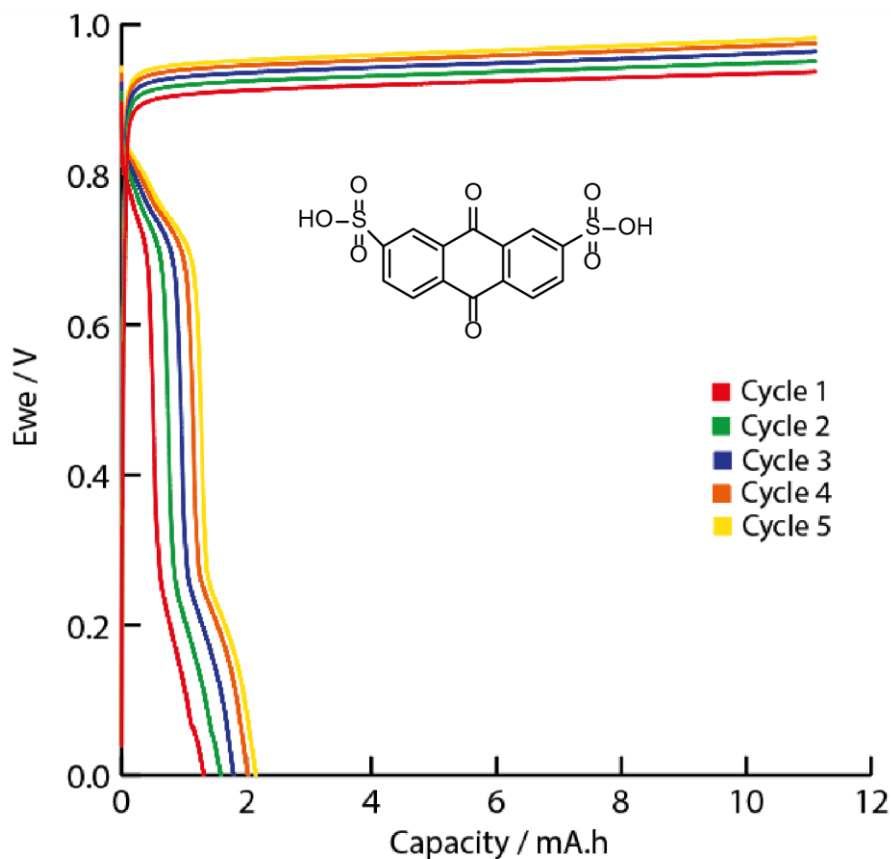


Figure 47 - Voltage vs Capacity for **1a** in H_2SO_4 coupled with HBr/Br_2

To provide further scope to the versatility of **11d**, an all-organic experiment was conducted utilising a 100 mM solution of **11d** in 0.1 M H_2SO_4 coupled with a 100 mM solution of **2a** shown below in Figure 48 in H_2SO_4 . **2a** was selected as a catholyte as it can undergo a two electron, two proton oxidation/reduction shown below in Figure 49 which matches that of **11d** and exhibits this behaviour at +0.66 V vs. SCE in 1M KCl which roughly correlates to +0.69 V vs. Ag/AgCl. ^[65] This thus gives a theoretical E_{cell} of 1.371 V although the experimental value for this may differ. **2a** was selected not only because it possesses a two electron, two proton redox reaction, but also compared to HBr/Br_2 it is less corrosive making it easier to work with in flow battery systems.

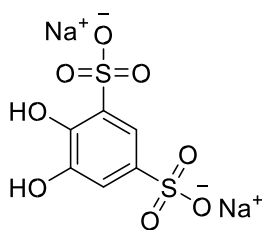


Figure 48 - Structure of **2a**

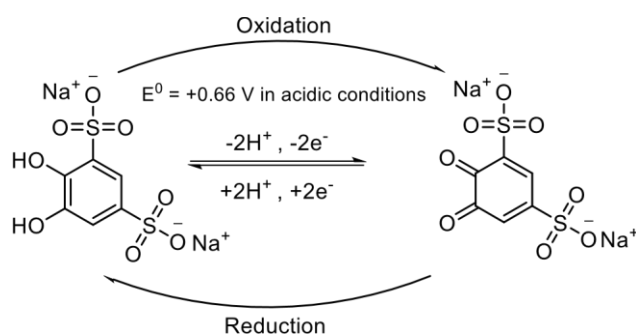


Figure 49 - Redox Pathway of **2a**

Figure 51 (graph) below is the data from this all-organic experiment. As the graph suggests this experiment was run over a period of three cycles, within these three cycles an overall charging capacity fade of ~81% was observed, yielding an average current efficiency of 21%. This vast decrease in capacity could be the result of potential side-reactions occurring within one of the electrolytes. One such reaction is highlighted in the Xu et al. paper published in 2010^[65], speculating that the first electro-oxidation of **2a** may be a four-electron reaction, and following this the molecule undergoes Michael addition of H₂O at position four of the molecule in the form of a hydroxyl moiety when in highly acidic conditions (shown below in Figure 50) and that subsequent oxidations take form of two-electron reactions.

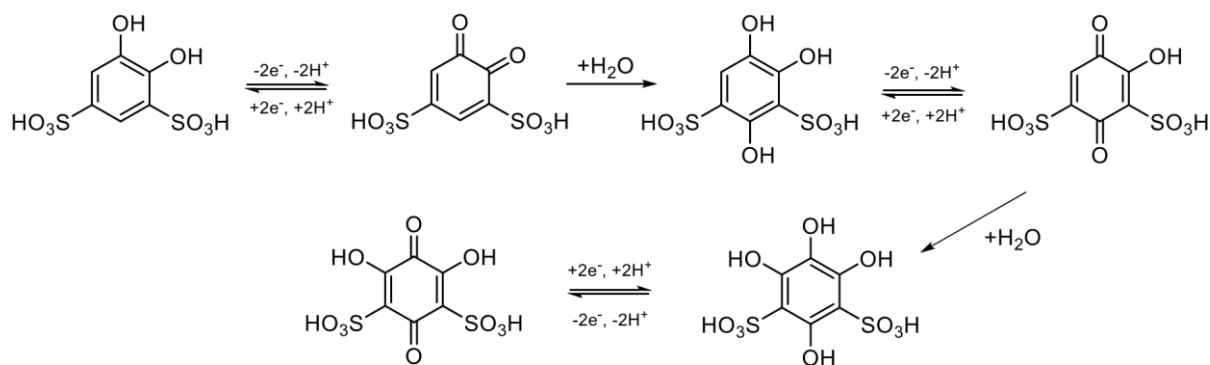


Figure 50 - The speculated pathway of Michael addition of H_2O to **2a** when oxidised ^[65]

As a result of these side-reactions it may hinder the reversibility and/or reduce the scale of the redox reaction of either molecule and be the cause of this observation.

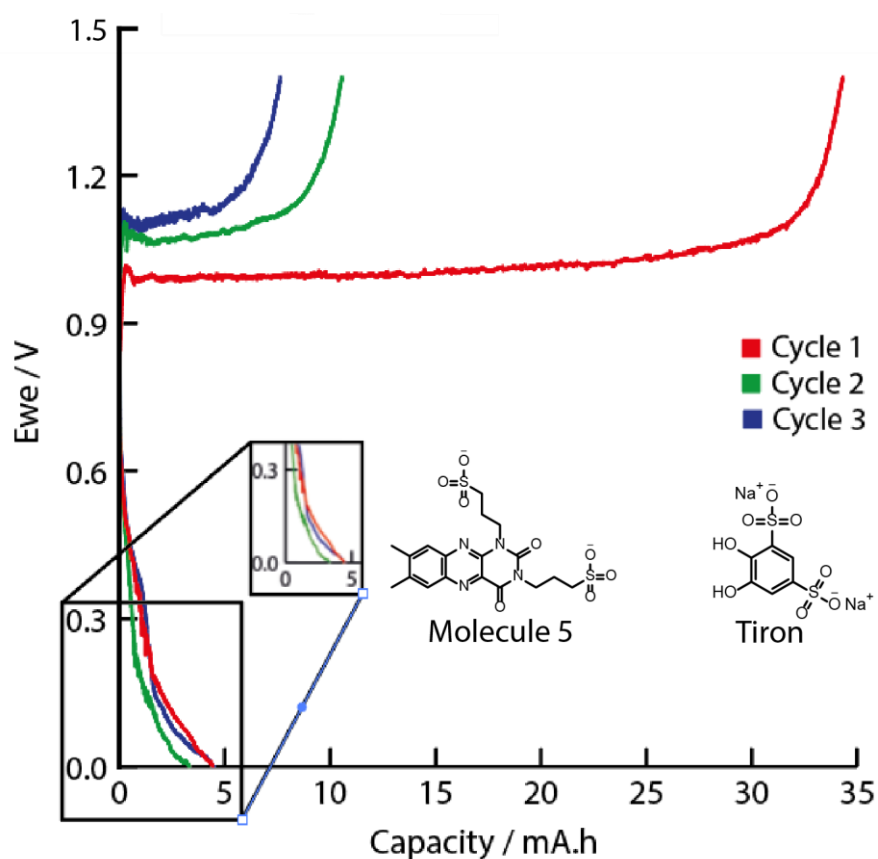


Figure 51 - Voltage vs. Capacity for **11d** in H_2SO_4 coupled with **2a** in H_2SO_4

After these subsequent experiments aiming to broaden and explore the options available for the utilisation of **11d** within flow systems. A final experiment was run, coalescing the ideal parameters that had been obtained from various experiments but returning to the initial couple of a 100 mM solution of **11d** in 0.1 M H₂SO₄ vs. an equal concentration of HBr/Br₂ charged at 10 mA and discharged at -10 mA. A capacity gate was included of 55.6 mA.h (200 C) calculated from the theoretical capacity of the solution to prevent ‘overcharging’ as seen in previous experiments. This system is estimated to have an E_{cell} of 1.608 V, however this uses a value of 870 mV for the HBr/Br₂ couple vs Ag/AgCl – this value may not be concurrent with actual values of HBr/Br₂ vs Ag/AgCl in acidic conditions and has been calculated from the E₀ value for Br₂/Br⁻ vs. SHE, so actual E_{cell} values may be lower. Figure 52 below illustrates the results of this experiment. The initial cycle charges to a capacity of 48.4 mA.h, 87 % of the maximum theoretical value and discharges 17.9 mA.h, yielding a current efficiency of 36.5 %. Subsequent cycles demonstrate a relatively constant capacity fade; however, the discharge capacity of the system remains constant throughout. Between the highest and lowest charge capacities a capacity fade of 20.3 % was observed. Over the seven cycles an average current efficiency of 44 % was observed, due to discharging capacity remaining relatively constant, whilst the charging capacity decreased.

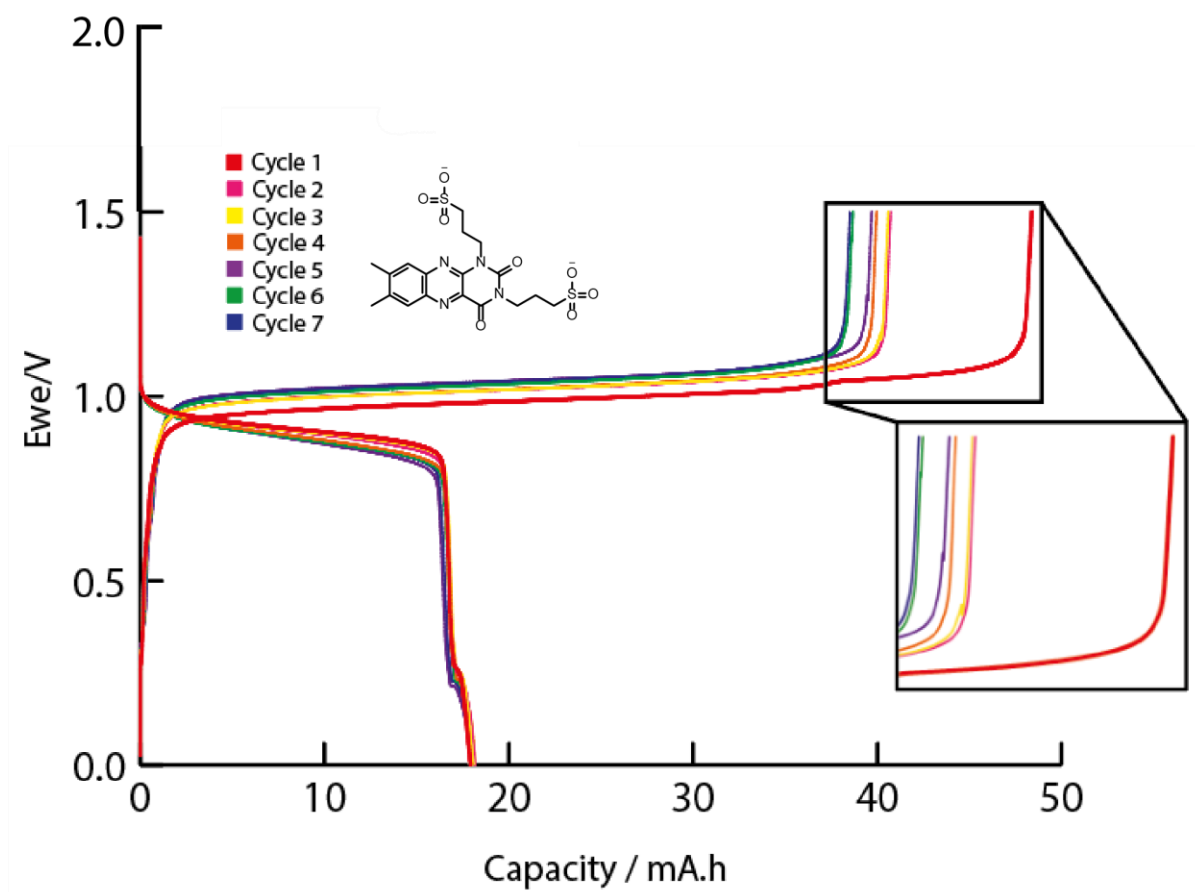


Figure 52 - Cell Voltage vs. Capacity for **11d** in H_2SO_4 coupled with HBr/Br_2 at 10 mAs^{-1}

Although the current efficiency of this system presented was below 50% and an 18% capacity fade was observed, this experiment yielded the most promising results from those that were conducted. After the initial cycles, the charging capacity does drop significantly however, after the second cycle it becomes relatively stable only dropping again significantly in the sixth cycle where it stabilises one more. These seven cycles (eight including an initial acclimatisation cycle) were conducted over a period of 48 hours, with each cycle taking 6 hours to complete. Given more time, it could be theorised that the charging capacity would eventually fade to match that of the discharging capacity – it could then be expected that both these values would fade proportionally until the system fails although the total of number of cycles required for this to occur is unknown.

Throughout all of the flow battery experiments presented for **11d** and the one presented of **1a**; it is displayed that the current efficiency is relatively poor in the fact that the energy inputted into the system is never fully retrieved. There are a number of factors that could affect this, the molecule itself in this case **11d** is reducing to an irreversible reduced state – which would be observed in cyclic voltammetry testing unless this decomposition is happening on a much slower timescale than CV and remaining unnoticed although this would then be noticed by depreciation in capacity per cycle for each subsequent charge in the flow battery testing, which it is not, especially in the case of the discharge capacity. On the other hand, this could be due to effects within the battery system used unrelated to the molecules/solutions. Given that the same inefficiency was observed within the **1a** experiment this is the most likely cause. The pump that was used to cycle solutions around was limited to a flow rate of 40 mL/min with the tubing that was used in conjunction with it, this along with the relatively low concentration of the electrolytes introduces the effects of mass transport limitations on the system. The effects of mass transport limitations could imply that reduced or inversely oxidised states of molecule **5** were not flowing through the system as fast as they were being reduced/oxidised, leading to an early cut-off for both charging and discharging capacities. This theory of the limitations of mass transport on the system is reinforced by physical observations of the system, specifically that of the experiment ran in figure 52. When first making up the solution of **11d**, the solution is bright yellow in colour the molecule is then reduced when charging and presents a brown colour. The colour of the solution of **11d**, never fully returned to its original colour and instead finished as a dark orange solution, this resulting colour could be an indication that the reduced species was still present in the solution and that it had not all been oxidised back to its original state. Future work would include analysis of the reservoir solutions via UV/Vis spectroscopy to directly probe what is happening. A further consideration behind this colour was that bromine from the adjacent fluid circuit was crossing over into the circuit containing **11d** –

which could have also been identified via further experimentation with UV/Vis or other spectroscopy techniques. Furthermore, it was observed throughout the flow battery experiment that osmosis from the catholyte to the anolyte via the cell membrane was occurring. The rate at which osmosis was occurring was thought to be due to slight differences in concentration between the two solutions, which was refined; however, this osmotic effect still occurred only slower. A theory behind this is that during the charging process the total number of ions on the anodic side of the cell decreases, whereas this total number on the cathodic side stays constant – this is due to hydrogen existing in an ionic state when in HBr (H^+/Br^-), but then in a covalent state on the reduced flavin (**11d**) as seen previously in the schematic diagram in Figure 44 (p.57). Comparing this observation with known systems of similar types, no such phenomenon was reported in the AQDS/HBr system ^[42] – although these two systems operate at different concentrations and thus the effects of osmosis may be more noticeable at lower electrolyte concentrations.

Chapter 4 - Conclusion

The combined aims of this paper were to explore the redox activity of organic molecules and to assess their use within a redox flow system. Those organic molecules took the form of those inclusive of the nitroxyl radical and the derivatives of the naturally occurring molecule **6a**. The former of which proved difficult to synthesise to a degree that was suitable to conduct cyclic voltammetry experiments on and thus, also battery testing. The methods that were followed to achieve products inclusive of the nitroxyl radical included strict atmospheric controls, which could have been deviated from resulting in both poor yields and poor purities in products from the synthetic attempts. Unfortunately, no conclusive evidence for their redox activities and thus their usefulness within a flow battery system were found for both the chosen target molecules. (**8a** and **10a**) With these molecules failing to achieve any of the three main aims of this research, the focus of the project was then changed towards flavin derivatives, due to their natural abundance and inherent redox activity. Experiments conducted on these molecules, specifically **11d** were conclusive and showed positive results confirming the redox activity and reversible electrochemical nature of this molecule, which allowed for further experimentation in a flow battery system coinciding with both the second and third main aims. These subsequent battery experiments were conducted to initially test the performance of **11d**, against a known redox couple of HBr/Br_2 – which proved positive. However, the system suffered from relatively low current efficiencies and high charging capacity fades – these results however could be a reflection on the battery system itself rather than the performance of the molecule itself, with factors such as mass transport limitations with the flow system being a potential detriment to these results. Further flow battery experimentation was conducted on **11d**, utilising different redox couples including HI to compare these results against the HBr/Br_2 couple. As well as the use of the organic molecule Tiron, to form an all-organic system – these two experiments served to expand the scope and show the versatility of **11d**

when utilised within a flow battery system. However, these experiments also suffered from low current efficiencies and high charging capacity fades.

Ultimately, the aims of the research conducted as part of this paper were to successfully synthesise and study the redox activity of novel organic molecules for RFBs. Both of these aims have been achieved under the synthesis of and subsequent experiments conducted **11d**, despite achieving less than optimum outcomes in terms of battery testing. **11d** has been shown to be a viable molecule for utilisation within a flow battery system and is the first reported example of an alloxazine-based RFB operating at acidic pH, despite the presented results and given more time to optimise the flow system itself and find the root of the issue to solve the disparity between the charging and discharging capacity – these results could be improved and the viability of **11d** therefore increased and thus fulfilling the criteria for aim three.

4.1 Future Work

Further work would seek to optimise the **11d**||HBr/Br₂ acidic condition flow battery. With efforts focusing on seeking the reason behind both the sharp charging capacity fade between the first and subsequent cycles – including UV/Vis spectroscopy on the resultant reservoir contents to see if any potential crossover has occurred. In addition, refinement of concentration differences between these two solutions – in an attempt to negate the osmosis that was observed to happen between the reservoirs, either by means of increasing concentrations of both solutions so that they are easier to work with or the use of precise instrumentation to correct these differences. Running this system at higher concentrations, would give a better understanding of the limitations and thus capabilities of **11d** itself and seek to remove the detrimental effects of any concentration and instrumentation limitations that may be affecting the system at this small scale. Future work would also include accurate experimental readings for counter-reactions vs. Ag/AgCl electrodes to accurately determine E_{cell} values. In addition

to the optimisation of the **11d** flow battery system, further and complete characterisation of the compounds synthesised as part of this research within these working systems would be carried out.

Chapter 5 - Experimental Methodology

Synthetic Methods

Syntheses of **9a** ^[61]

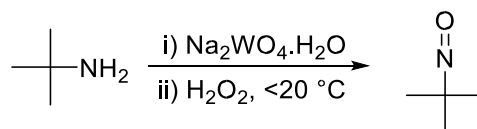


*Figure 53 - Reaction Pathway for Synthesis of **9a***

$\text{Na}_2\text{WO}_4\cdot 2\text{H}_2\text{O}$ (4.029 g , 13 mmol) and tBuNH_2 (53 cm^3 , 0.50 mol) were dissolved in H_2O (50 cm^3). The mixture was cooled in an ice bath. H_2O_2 (21% , 160 cm^3 , 6.82 mol) was then added over 80 minutes, whilst keeping the internal temperature below 20 $^\circ\text{C}$. The reaction was then allowed to stir for a further 30 minutes at 20-25 $^\circ\text{C}$. The mixture was then placed in the fridge, and crystallisation occurred overnight. The supernatant was decanted off and blue crystals were isolated. Both the crystals $^1\text{H-NMR}$ (400 MHz, CDCl_3): $\delta = 1.61$ (d), 1.26 (s). and supernatant liquid $^1\text{H-NMR}$ (400MHz, CDCl_3): $\delta = 1.58$ (s), 1.56 (s), 1.46 (s), 1.26 (s), 1.21 (s), 1.12 (s). were analysed utilising NMR spectrometry. Distillation of the resultant aqueous solution at 80 $^\circ\text{C}$ resulted in a further yield of blue needle-like crystals $^1\text{H-NMR}$ (400 MHz, CDCl_3): $\delta = 1.34$ (s), 1.31 (s), 1.21 (s), 1.01 (s), 0.97 (s), 0.78 (s).

Syntheses of **8a** ^[60]

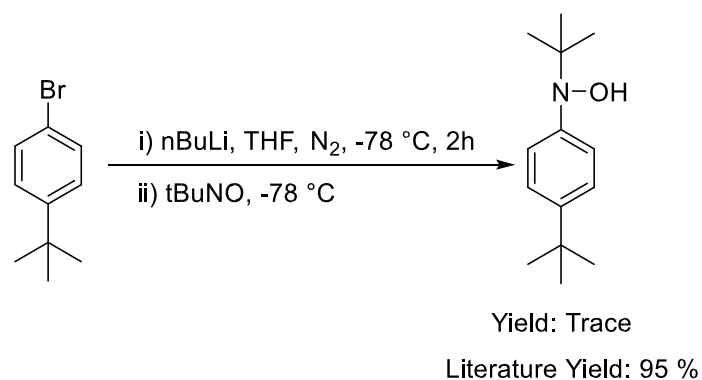


Figure 54 - Reaction Pathway for Step 1 of the Synthesis of **8a**

1-bromo-4-tertbutylbenzene (0.175 mL, 1.0 mmol) was dissolved in THF under a nitrogen atmosphere. The mixture was then cooled to -78 °C. n-BuLi (0.75 mL, 8.0 mmol) was then added dropwise allowing the resultant mixture to warm to 0 °C for 2 h whilst stirring. The mixture was then cooled to -78 °C, then **9a** crystals (0.105 g, 1.2 mmol) were added and allowed to warm to ambient temperature. The reaction was quenched with ice and extracted with diethyl ether (2 x 10 mL). The resultant mixture was dried with MgSO₄, filtered and then the diethyl ether removed, yielding a yellow powder (trace).

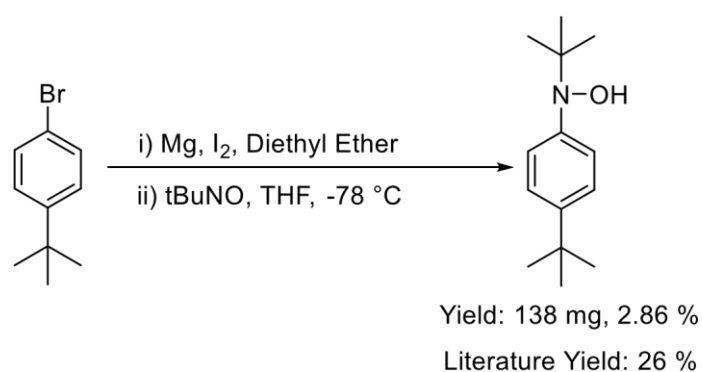
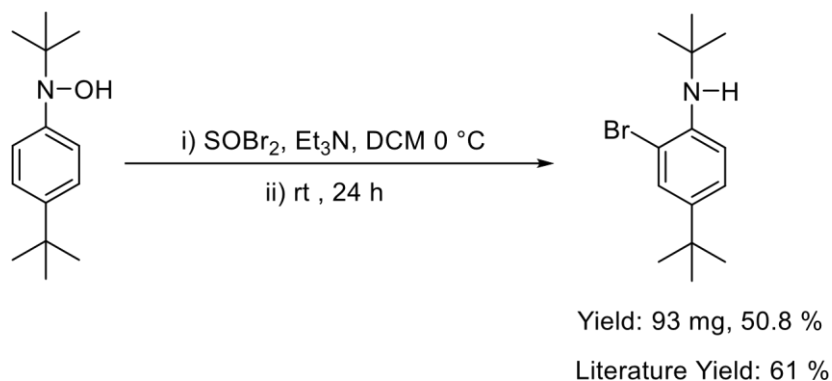


Figure 55 - Secondary Reaction Pathway for Step 1 of the Synthesis of **8a**

Mg (0.547 g, 22.5 mmol) and I₂ (one crystal) were added to a vessel and 1-bromo-4tertbutylbenzene (4 mL, 23.0 mmol) dissolved in diethyl ether (50 mL) was added slowly whilst heating and stirring the reaction vessel. Resultant mixture allowed to stir for a further 30 minutes. **9a** (1.902 g, 21.8 mmol) dissolved in THF (8 mL) was then added cautiously and allowed to stir overnight. The reaction mixture was then quenched with ice/H₂O and filtered. The organic layer was separated, and aqueous layer extracted with diethyl ether (3 x 10 mL). The extracted mixture was then filtered through cotton and concentrated. Yielding 2.024 g of orange oil as a product. This organic product was further separated utilising column chromatography (19:1 , petroleum ether : ethyl acetate). The combined fractions were concentrated yielding a red oil, 138 mg (2.86 %). ¹H-NMR (400MHz, CDCl₃): δ = 7.34 (d), 7.22 (s), 7.20 (s), 7.19 (s), 7.17 (s), 7.10 (d), 1.53 (s – broad), 1.29 (s), 1.25 (s), 1.23 (d), 1.20 (d), 1.07 (s), 0.98 (d). ¹³C-NMR (400 MHz, CDCl₃): δ = 124.41, 124.13, 77.46, 77.14, 76.82, 34.36, 31.45, 25.91).

Synthesis of **8a** (Cont.)



*Figure 56 - Reaction Pathway for Step 2 of the Synthesis of **8a***

To a reaction vessel cooled in ice containing the product from Step 1 of the synthesis of **8a** (0.135 g, 0.61 mmol) dissolved in DCM (5 mL), Et₃N (0.07 mL,) and SOBr₂ (0.04 mL,) was added and allowed to stir for 24 hours. Diethyl ether (20 mL) was added to the reaction vessel, along with H₂O (10 mL) to dissolve precipitated content of the reaction vessel. The reaction mixture was then separated, and the organic layer washed with NaOH (10 mL, 5%) to aid separation. The organic layer was then washed with H₂O (7 x 10 mL), the resultant extract was dried with Na₂SO₄ and then concentrated, yielding 93 mg (50.8 %) of a brown oil. ¹H-NMR (400 MHz, CDCl₃): δ = 7.36 (d), 7.09 (d), 7.07 (d), 6.85 (s), 6.83 (s), 4.09 (s – broad), 3.40 (q), 1.31 (s), 1.19 (s).

Synthesis of **10a** [66]

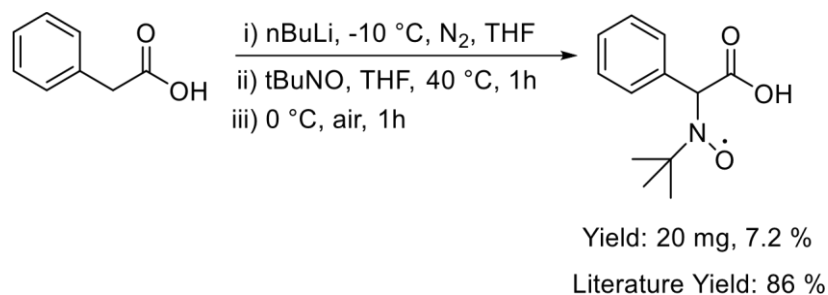


*Figure 57 - Reaction Pathway for Synthesis of **10a***

Phenylacetic acid (170 mg , 1.25 mmol) was dissolved in THF (2 mL) and then cooled to -10 °C. 1.6M n-BuLi (1.7 mL , 18.39 mmol) was then added dropwise under N₂ and reaction mixture stirred and heated to 40 °C for 1 h. Reaction mixture was then cooled to -78 °C. **9a** (130 mg , 1.95 mmol) dissolved in THF (2 mL) was then added slowly and reaction mixture allowed to warm to ambient temperature (23 °C~) whilst stirring overnight. Reaction mixture was then cooled to 0 °C, opened to air and stirred for a further 1 h. Reaction mixture was then adjusted to pH 8 using chilled 1M HCl. Organic solvent evaporated and aqueous residue diluted with H₂O (5 mL). Resultant solution was washed with ether and then the aqueous layer was dried under vacuum for 12 h. Yielding 253 mg of yellow oil which was aired until dry. Dried product was then taken up in CHCl₃ (50 mL) and filtered. Resulting solution concentrated and dried. The product of which was then analysed via ¹H-NMR (400 MHz CDCl₃): 9.95 (s), 8.21 (dd – obscured), 7.99 (dd), 7.82 (dd), 7.64 (dd), 7.5-7.2 (cluttered), 3.56 (s), 1.55 (s), 1.40 (s), 1.31 (s), 1.25 (s). Phenylhydrazine was then added to a portion of dried product and analysed via ¹H-NMR (400 MHz, CDCl₃): δ = 7.14 (dd), 6.74 (d), 6.69 (d), 4.15 (s – broad), 1.51 (s), 1.38 (s), 1.18 (s), 1.12 (s). 253 mg of dried product extracted with Acetonitrile: Hexane, yielding 20 mg (7.2 %) of extracted product. Extracted product then dissolved in 0.1M NaOH (10 mL) and analysed via cyclic voltammetry.

Synthesis of 11a ^[67]

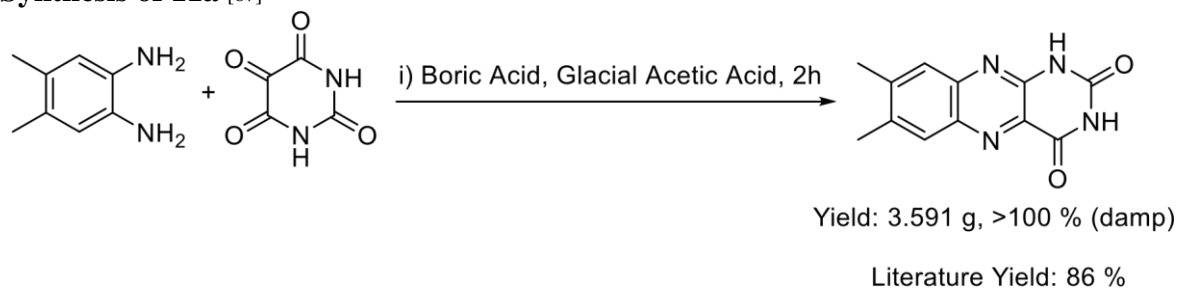
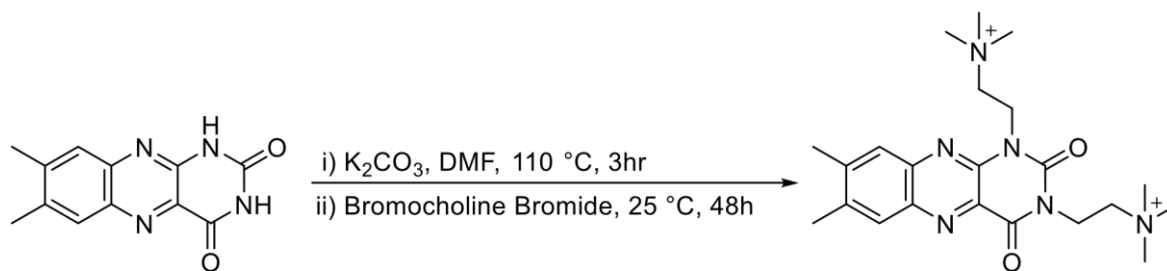


Figure 58 - Reaction Pathway for Synthesis of 11a

To a mixture of 4,5-dimethylbenzene-1,2-diamine (1.907 g , 14 mmol) dissolved in glacial acetic acid (75 mL), a solution of Alloxan monohydrate (2.241 g , 14 mmol) and boric acid (1.051 g , 17 mmol) also dissolved in glacial acetic acid (50 mL) that had been preheated to 55 °C was added and then allowed to stir at 25 °C for 2 hrs. Resultant precipitate was then filtered and washed with glacial acetic acid (20 mL) and diethyl ether (20 mL x 3) then dried. This gave 3.591 g (>100 %, residual solvent present) of deep yellow solid. ¹H-NMR (400 MHz, DMSO-d₆): δ = 11.91 (s – broad), 11.70 (s – broad) 7.92 (s), 7.71 (s), 3.35 (s), 2.47 (s), 1.91 (s)

Synthesis of 11b



Theoretical Yield: 1.73 g

Figure 59 - Reaction Pathway for Synthesis of Lumichrome-bis(Ethyltrimethylamine)

11a (1.011 g , 4.17 mmol) and K_2CO_3 (1.001 g , 7.24 mmol) were dissolved in DMF (50 mL). The solution was then heated to 110 °C and stirred for 3 hrs. The reaction mixture was then filtered and washed with DMF (10 mL x 3). The deprotonated product was dried and then dissolved in DMF (100 mL), bromocholine bromide (1.257 g , 6.83 mmol) was then added and reaction mixture was stirred for 48 hrs at 25 °C. The reaction mixture was then filtered and washed with DMF (10 mL x 3). 1H -NMR (400 MHz, D_2O): δ = 7.29 (d), 7.02 (s), 6.87 (s), 4.62 (t), 4.46 (t), 3.59 (t), 3.26 (d), 3.23 (s), 2.21 (d), 2.14 (d). Product then redissolved in DMF (50 mL), bromocholine bromide (0.612 g, 3.32 mmol) added and reaction mixture stirred for 48hrs at 25 °C. The resultant product was then filtered and dried. (trace) 1H -NMR (400 MHz, D_2O): δ = 7.58 (d), 4.44 (t), 3.58 (t), 3.53 (t), 3.19 (d), 3.15 (s), 3.04 (s), 2.85 (s), 2.69 (s), 2.31 (d), 2.05 (d). ^{13}C -NMR (400 MHz, D_2O): δ = 150.2, 149.8, 144.9, 142.7, 141.2, 137.6, 128.2, 126.4, 124.4, 54.1, 53.4, 53.3, 19.9, 19.8, 19.2, 19.1. FTIR (neat): 1615 cm^{-1} (b), 1575 cm^{-1} (s), 1445 cm^{-1} (s), 1360 cm^{-1} (b), 1300 cm^{-1} (s), 1245 cm^{-1} (s), 1000 cm^{-1} (s), 815 cm^{-1} (s), 700 cm^{-1} (s), 545 cm^{-1} (s).

Synthesis of 11c

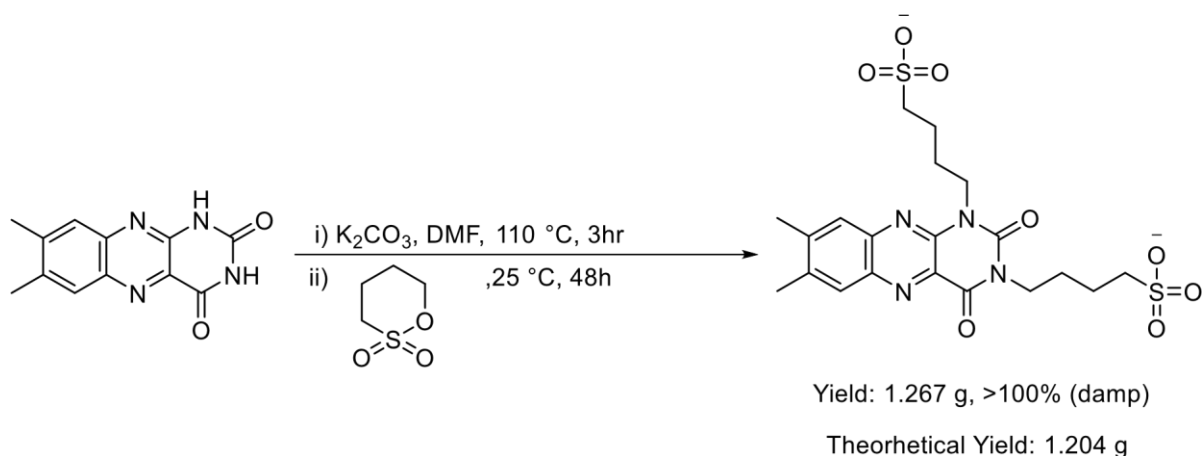


Figure 60 - Reaction Pathways for Synthesis of Lumichrome-bis(Butylsulfonate)

11a (0.552 g , 2.35 mmol) and K_2CO_3 (0.6 g , 4.34 mmol) were dissolved in DMF (50 mL) then heated at 110 °C and stirred for 3 hrs. The solution was then allowed to cool to 25 °C. The resulting precipitate was filtered and washed with DMF (20 mL). The deprotonated alloxazine was redissolved in DMF (50 mL), and 1,4-butane sultone (0.700 g , 5.14 mmol) was added to the mixture and allowed to stir for 48 hrs. The resulting precipitate was then filtered and washed with DMF (30 mL), yielding 1.267 g (>100 %) of yellow solid – damp with DMF. 1H -NMR (400 MHz, D_2O): δ = 7.86 (s), 7.24 (s), 7.07 (s), 2.94 (s), 2.78 (s), 2.24 (d).

Synthesis of 11d

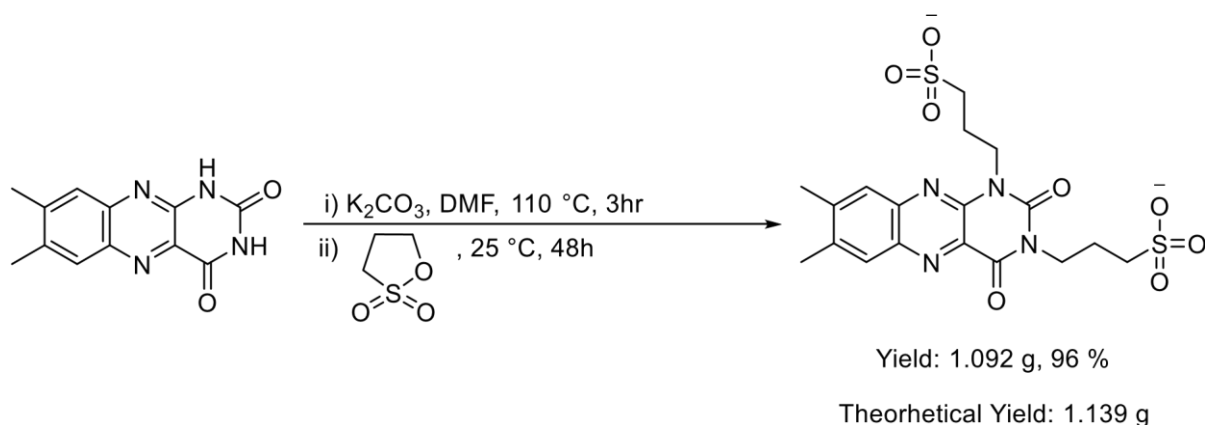


Figure 61 - Reaction Pathway for Synthesis of Lumichrome-bis(Propylsulfonate)

11a (0.552 g , 2.35 mmol) and K_2CO_3 (0.600 g , 4.34 mmol) were dissolved in DMF (50 mL) then heated at 110 °C and stirred for 3 hrs. The solution was then allowed to cool to 25 °C, then filtered and washed with DMF (20 mL). The deprotonated product was redissolved in DMF (50 mL), then to the reaction mixture 1,3-propane sultone (0.6 g , 4.91 mmol) was added and allowed to stir for 48 hrs. The resulting precipitate was then filtered and washed with DMF (30 mL), yielding 1.092 g (96 %) of dry yellow solid. 1H -NMR (400 MHz, D_2O): δ = 7.86 (s), 7.82 (d), 4.43 (t), 4.16 (t), 2.94 (s), 2.78 (s), 2.47 (d). ^{13}C -NMR (400 MHz, D_2O): δ = 160.6, 150.6, 147.2, 143.7, 141.8, 127.3, 127.2, 126.1, 62.6, 50.4, 48.6, 47.2, 41.4, 22.6, 22.5, 20.1, 19.4, 18.1. FTIR (dry): 1645 cm^{-1} (s), 1545 cm^{-1} (s), 1175 cm^{-1} (b), 1030 cm^{-1} (s), 745 cm^{-1} (s), 610 cm^{-1} (s), 575 cm^{-1} (s), 530 cm^{-1} (s).

Standard Synthetic Conditions

Within all of the syntheses listed above, glassware that had been through Acid/Base wash was used to ensure no contaminants were present during synthetic attempts. Where the synthetic method included reagents that are sensitive to water and/or required strict atmospheric controls; dry solvents were utilised e.g. The syntheses of both 8a and 10a requiring the use of n-BuLi. All other syntheses involved the use of general lab solvents and only utilised dry solvents when preparing the sample for analysis by both NMR and CV.

Spectrometry

Both ^1H and ^{13}C NMR were conducted in appropriate deuterated solvents to ensure complete solubility of the analyte. These spectra were obtained utilising the same 400MHz Bruker Spectrometer and contained within prewashed and dried NMR Tubes.

IR Spectroscopy was carried out utilising a Shimadzu Fourier Transform IR Spectrophotometer. In some cases these analyses were carried out in solid form where appropriate, or in the cases where a solvent was required – the analyte was dissolved within a dry solvent.

Electrochemical Analysis

All electrochemical analysis was carried out utilising a 'BioLogic VMP3 Potentiostat' for data acquisition and the EC-Lab software for data visualisation.

Cyclic Voltammetry (CV)

Standard operating procedures for these analyses included the use of an Ag/AgCl reference electrode, a glassy carbon working electrode (3 mm² tip) and a platinum wire counter electrode. The glassy carbon working electrode was polished three times in succession, each time reducing the grit size from 6 μm to 1 μm using a nano diamond polishing solution and finally

0.05 μm using an alumina polishing solution. Furthermore, each test solution was thoroughly degassed with nitrogen prior to analysis via cyclic voltammetry. For cyclic voltammetry analysis, 15 mg of sample was dissolved in 15 cm^3 of electrolyte unless otherwise stated.

Flow Battery Testing

All flow battery experiments were carried out utilising standard equipment throughout, including a MasterFlex peristaltic pump and an ElectroCell 5 cm^2 these cells are commercially available flow cells.

The ElectroCell utilises PTFE flow frames, EPDM, FPM (Viton) sealing gaskets and graphite electrodes. This cell setup was used in tandem with carbon felt electrodes and either Fumapem FAP-450 (For anion exchange environments) or Fumapem F-930 (For cation exchange environments) acting as the ion exchange membrane. This cell features an internal volume of 10 mL, a 0.7~ mm electrode gap range and serpentine flow fields, which when running these experiments were set up parallel to each other.

Bibliography

- [1] UK Renewable Energy Roadmap, Department of Energy & Climate Change, 2011, https://assets.publishing.service.gov.uk/government/uploads/system/uploads/attachment_data/file/48128/2167-uk-renewable-energy-roadmap.pdf, (accessed 16/12/2020)
- [2] T. Kim, W. Song, D. Son, L. K. Ono, Y. Qi, J. Mater. Chem. A, 2019, **7**, 2942-2964
- [3] R. Chen, S. Kim, Z. Chang, in Redox – Principles and Advanced Applications, ed. M. A. A. Khalid, IntechOpen, 2017, ch. 5, pp. 103-118.
- [4] 2020 Grid Energy Storage Technology Cost and Performance Assessment, <https://www.pnnl.gov/sites/default/files/media/file/Final%20-%20ESGC%20Cost%20Performance%20Report%2012-11-2020.pdf>, (accessed 20/01/2021)
- [5] M. Kapoor, R. K. Gautam, V. K. Ramani, A. Verma, Chem. Eng. J., 2020, **379**, 122300
- [6] McEvoy's Handbook of Photovoltaics, Academic Press, Cardiff University, 3rd edn., 2018, ch. II-3-D, pp. 915-928
- [7] IRENA – Climate Policy Drives Shift to Renewable Energy - https://www.irena.org//media/Files/IRENA/Agency/Topics/Climate-Change/IRENA_Climate_policy_2017.pdf, (accessed 20/01/2021)
- [8] Dalian 1.2MW/3.2MWH Vanadium RFB - <http://www.rongkepower.com/Uploads/file/20170217/58a6a95f0206c.pdf>, (accessed 17/05/202)
- [9] ZMB2 Flow Battery Datasheet, <https://redflow.com/wpcontent/uploads/2019/10/Redflow-ZBM2-datasheet-1910-Public-Web.pdf>, (accessed 16/12/202)
- [10] B. Huskinson, M. P. Marshak, C. Suh, S. Er, M. R. Gerhardt, C. J. Galvin, X. Chen, A. Aspuru-Guzik, R. G. Gordon, M. J. Aziz, Nat., 2014, **505**, 195-198
- [11] K. Lourenssen, J. Williams, F. Ahmadpour, R. Clemmer, S. Tasnim, J. Energy Storage, 2019, **25**, 100844
- [12] P. J. Cabrera, X. Yang, J. A. Suttill, K. L. Hawthorne, R. E. M. Brooner, M. S. Sanford, L. T. Thompson, J. Phys. Chem. C, 2015, **119**, 15882-15889
- [13] IRENA, Electricity Storage and Renewables: Costs and Markets to 2030, International Renewable Energy Agency, Abu Dhabi, 2017, https://www.irena.org/-/media/Files/IRENA/Agency/Publication/2017/Oct/IRENA_Electricity_Storage_Costs_2017.pdf, (accessed 17/05/202)
- [14] Dalian 200MW/800 MWH Vanadium RFB, <http://www.rongkepower.com/Uploads/file/20170217/58a692efc334f.pdf>, (accessed 17/05/202)
- [15] Voltstorage.com, <https://voltstorage.com/>, (accessed 16/12/2020)
- [16] L. Li, S. Kim, W. Wang, M. Vijayakumar, Z. Nie, B. Chen, J. Zhang, G. Xia, J. Hu, G. Graff, J. Liu, Z. Yang – Adv. Energy Mater., 2011, **1**, 394-400
- [17] Bushveld Minerals: About Vanadium, <https://www.bushveldminerals.com/aboutvanadium/>, (accessed 15/01/2021)

- [18] Vanadium Price, <https://www.vanadiumprice.com/>, (accessed 15/01/2021)
- [19] Toxicity of Vanadium Pentoxide, https://rais.ornl.gov/tox/profiles/vanadium_f_V1.html, (accessed 15/01/2021)
- [20] Formal Toxicity Study for Vanadium, https://rais.ornl.gov/tox/profiles/vanadium_f_V1.html, (accessed 15/01/2021)
- [21] L. H. Thaller, NASA Tech. Memorandum, Electrically Rechargeable Redox Flow Cells, San Francisco, January, 1974
- [22] M. Lopez-Atalaya, G. Codina, J. R. Perez, J. L. Vasquez, A. Aldaz, J. Power Sources, 1992, **39**, 147-154
- [23] C. R. Horne, S. Nevins, EnerVault – 2014 DOE Energy Storage Peer Review, https://www.sandia.gov/essssl/docs/pr_conferences/2014/Thursday/Session7/01_Nevins_Sheri_IRONCHROMIUM_REDOX.pdf, (accessed 16/12/2020)
- [24] W. Ruan, J. Mao, S. Yang, C. Shi, G. Jia, Q. Chen, Chem. Comm., 2020, **56**, 3171
- [25] Y. K. Zeng, T. S. Zhao, L. An, X. L. Zhou, L. Wei, J. Power Sources, 2015, **300**, 438-443
- [26] Y. Shiokawa, H. Yamana, H. Moriyama, J. Nucl. Sci. Tech., 2000, **37**, 253-256
- [27] Y. Shiokawa, T. Yamamura, K. Shirasaki, J. Phys. Soc. Jpn., 2006, **75**, 137-142
- [28] United States Nuclear Regulatory Commission FAQs, <https://www.nrc.gov/waste/llwdisposal/llw-pa/uw-streams/bg-info-du.html>, (accessed 16/12/2020)
- [29] Energystorage.org, <https://energystorage.org/why-energy-storage/technologies/zincbromine-znbr-flow-batteries/>, (accessed 16/12/2020)
- [30] ZBM2 Flow Battery Datasheet - Redflow.com, <https://redflow.com/wpcontent/uploads/2019/10/Redflow-ZBM2-datasheet-1910-Public-Web.pdf>, (accessed 16/12/2020)
- [31] R. Kim, S. Yuk, J. Lee, C. Choi, S. Kim, J. Heo, H. Kim, J. Mem. Sci., 2018, **564**, 852858
- [32] Performance Testing of Zinc-Bromine Flow Batteries for Remote Telecom Sites, <https://www.sandia.gov/ess-ssl/publications/SAND2013-2818C.pdf>, (accessed 20/01/2021)
- [33] W. Lu, C. Xie, H. Zhang, X. Li, Chem. Sus. Chem., 2018, **11**, 3996-4006
- [34] Solarquote.com.au, <https://www.solarquotes.com.au/blog/redflow-zbm2-zcell-newsmb0838/>, (accessed 16/12/2020)
- [35] Redflow.com, [-storage-system-cuts-home-powerbill-by-80/#more-8336](https://www.redflow.com/news/storage-system-cuts-home-powerbill-by-80/#more-8336), (accessed 16/12/2020)
- [36] US Pat., 7625663B2, 2001
- [37] Sandia.gov, https://www.sandia.gov/ess-ssl/EESAT/2002_papers/00024.pdf, (accessed 16/12/2020)
- [38] X. Yu, A. Manthiram, Adv. Sustainable Syst., 2017, **1**, 2366-7486

- [39] J. Winsberg, T. Hagemann, T. Janoschka, M. D. Hager, U. S. Schubert, *Angewandte Chemie*, 2017, **56**, 686-711
- [40] B. Hu, J. Luo, M. Hu, B. Yuan, T. L. Liu, *Angewandte Chemie*, 2019, **131**, 16782-16789
- [41] K. Gong, Q. Fang, S. Gu, S. F. Y. Li, Y. Yan, *Energy Environ. Sci.*, 2015, **8**, 3515-3530
- [42] B. Huskinson, M. P. Marshak, C. Suh, S. Er, M. R. Gerhardt, C. J. Galvin, X. Chen, A. Aspuru-Guzik, R. G. Gordon, M. J. Aziz, *Nat.*, 2014, **505**, 195-198
- [43] D. G. Kwabi, K. Lin, Y. Ji, A. Aspuru-Guzik, R. G. Gordon, M. J. Aziz, *Joule*, 2018, **2:9**, 1894-1906
- [44] B. Yang, L. Hooper-Burkhardt, S. Krishnamoorthy, A. Murali, G. K. S. Prakash, S. R. Narayanan, *Journal of The Electrochemical Society*, 2016, **163**, 1442-1449
- [45] S. Jin, Y. Jing, D. G. Kwabi, Y. Ji, L. Tong, D. D. Porcellinis, M. Goulet, D. A. Pollack, R. G. Gordon, M. J. Aziz, *ACS Energy Lett.* 2019, **4**, 1342-1348
- [46] K. Lin, Q. Chen, M. R. Gerhardt, L. Tong, S. B. Kim, L. Eisenach, A. W. Valle, D. Hardee, R. G. Gordon, M. J. Aziz, M. P. Marshak (2015). Alkaline quinone flow battery. *Science*, **349**, 1529-1532.
- [47] T. Liu, X. Wei, Z. Nie, V. Sprenkle, W. Wang, *Adv. Energy Mater.* 2016, **6**, 1501449
- [48] A. Ohira, T. Funaki, E. Ishida, J. Kim, Y. Sato, *ACS Appl. Energy Mater.*, 2020, **3**, 4377-4383
- [49] J. E. Nutting, M. Radice, S. S. Stahl, *Chem. Rev.*, 2018, **118**, 4834-4885
- [50] Y. Liu, M. Goulet, L. Tong, Y. Liu, Y. Ji, L. Wi, R. G. Gordon, M. J. Aziz, Z. Yang, T. Xu, *Chem*, 2019, **5**, 1861-1870
- [51] J. Winsberg, C. Stolze, S. Muench, F. Liedl, M. D. Hager, U. S. Schubert, *ACS Energy Lett*, 2016, **1**, 976-980
- [52] T. Janoschka, S. Morgenstern, H. Hiller, C. Friebe, K. Wolkersdörfer, B. Häupler, M. D. Hager, U. S. Schubert, *Polym. Chem.*, 2015, **6**, 7801-7811
- [53] A. Orita, M.G. Verde, M. Sakai, Y.S. Meng, *J. Power Sources*, 2016, **321**, 126-134
- [54] R. Bitsch, in *Encyclopedia of Food Sciences and Nutrition*, ed. B. Caballero, Elsevier, 2nd edn., 2003, ch. Riboflavin | Properties and Determination, pp. 4983-4989
- [55] S. V. Tatwawadi, K. S. V. Santhanam, A. J. Bard, *J. Electroanal. Chem.*, 1968, **17**, 411420
- [56] A. Orita, M. G. Verde, M. Sakai, Y. S. Meng, *Nat. Commun.*, 2016, **7**, 13230

- [57] K. Lin, R. Gómez-Bombarelli, E. S. Beh, L. Tong, Q. Chen, A. Valle, A. Aspuru-Guzik, M. J. Aziz, R. G. Gordon, *Nat. Energy*, 2016, **1**, 16102
- [58] O. A. Levitskiy, D. B. Eremin, A. V. Bogdanov, T. V. Magdesieva, *Eur. J. Org. Chem.*, 2017, **32**, 4726-4735
- [59] E. A. Karpushkin, N. A. Gvozdik, O. A. Levitskiy, K. J. Stevenson, V. G. Sergeyev, T.V. Magdesieva, *Colloid and Polymer Sci.*, 2019, **297**, 317-323
- [60] L. Marx, A. Rassat, *Tetra. Lett.*, 2002, **43**, 2613-2614
- [61] J.C. Stowell, *J. Org. Chem.*, 1971, **36**, 3055-3056
- [62] N. R. Ayyangar, U. R. Kalkote, P. V. Nikrad, *Tet. Lett.*, 1982, **23**, 1099-1102
- [63] M. M. Walczak, D. A. Dryer, D. D. Jacobson, M. G. Foss, N. T. Flynn, *J. Chem. Educ.*, 1997, **74**, 1195-1197
- [64] K. Gumus, A. Murray, University of Kent, Unpublished Work
- [65] Y. Xu, Y. Wen, J. Cheng, G. Cao, Y. Yang, *Electrochimica Acta*, 2010, **55**, 715–720
- [66] J. F. W. Keana, S. Pou, *J. Org. Chem*, 1989, **54**, 2417-2420
- [67] G. Gonzalo, C. Smit, J. Jin, A. J. Minnaard, M. W. Fraaije, *Chem. Commun.*, 2011, **47**, 11050-11052

